Deformation memory in the lithosphere: A comparison of damage-dependent weakening and grain-size sensitive rheologies

Lukas Fuchs[1] and Thorsten W. Becker[2,3]

[1] Institute for Geosciences, Goethe University, Frankfurt/Main, Germany

[2] Institute for Geophysics, Jackson School of Geosciences, The University of Texas at Austin, Austin, Texas, USA

[3] Department of Geological Sciences, Jackson School of Geoscience, The University of Texas at Austin, Austin, Texas, USA

Corresponding author: Lukas Fuchs, (lufuchs@geophysik.uni-frankfurt.de)

Key Points:

- Comparative analysis of strain-localization and damage-memory for grain-size dependent and strain/damage parameterized rheologies
- Identification of key ingredients of strain-localization and damage hysteresis and how to represent those in planetary-scale modeling
- Plastic strain softening enables hysteresis with a memory duration similar to grain growth at lithospheric temperature conditions

Abstract

Strain localization in the lithosphere and the formation, evolution, and maintenance of resulting plate boundaries play a crucial role in plate tectonics and thermo-chemical mantle convection. Previously activated lithospheric deformation zones often appear to maintain a "memory" of weakening, leading to tectonic inheritance within plate reorganizations including the Wilson cycle. Different mechanisms have been proposed to explain such strain localization, but it remains unclear which operate on what spatio-temporal scales, and how to best incorporate them in large-scale mantle convection models. Here, we analyze two candidates, 1), grain-size sensitive rheology and, 2), damage-style parameterizations of yield stress which are sometimes used to approximate the former. Grain-size reduction due to dynamic recrystallization can drive localization in the ductile domain, and grain growth provides a time-dependent rheological hardening component potentially enabling the preservation of rheological heterogeneities. We compare the dynamic weakening and hardening effects as well as the timescales of strength evolution for a composite rheology including grain-size dynamics with a pseudo-plastic rheology including damage- (or "strain"-) dependent weakening. We explore the implications of different proposed grain-size evolution laws, and test to which extent strain-dependent rheologies can mimic the weakening and hardening effects of the more complex micro-physical behavior. Such an analysis helps to better understand the parallels and differences between various strain-localization modeling approaches used in different tectonics and geodynamics communities. More importantly, our results contribute to efforts to identify the key ingredients of strain-localization and damage hysteresis within plate tectonics and how to represent those in planetary-scale modeling.

1 Introduction

The Earth's current mode of heat transport is by means of plate tectonics which, by definition, is characterized by relatively rigid plate interiors and narrow plate boundaries where deformation due to relative plate motions is localized. The lithosphere, i.e. the top, cold, strong thermo-chemical boundary layer of mantle convection, is thus broken up such that brittle or plastic processes reduce the effective strength of rocks (i.e. the viscosity in the case of fluid behavior) which would otherwise be huge if temperature-dependent creep were the only relevant deformation mechanism (e.g. Kohlstedt et al., 1995; Burov, 2011). For some aspects of convection models, such behavior can be approximated by "Byerlee" type visco-plasticity with a depth- or pressure-dependent yield stress (e.g. Moresi & Solomatov, 1998; Enns et al., 2005). However, the yield stresses that are needed to break a homogenous lithosphere in convection models are typically much lower than those expected from rock mechanics, and pure plasticity is on its own not progressively weakening and inherently without memory of deformation (e.g. Bercovici 2003; Tackley, 2000a).

It is likely that because of this lack of strain localization, visco-plastic rheologies in mantle convection models only yield approximately plate-like surface motions (e.g. Tackley, 2000b; van Heck & Tackley, 2008; Foley & Becker, 2009). The planform of surface motions seems to become more realistic when a low-viscosity asthenosphere (Tackley, 2000c; Richards et al., 2001; Höink et al., 2012), a strongly temperature-dependent viscosity (e.g. Coltice et al., 2017, 2019), a free surface and weak oceanic crust (Crameri et al., 2012), and/or the presence of strong continents (Coltice et al., 2012) is included within visco-plastic models. However, a velocity/strain-weakening or pseudo stick-slip, strain localizing rheology is still required to achieve appropriate levels of toroidal motion and hallmark features of plate tectonics such as transform faults offsetting spreading centers (e.g. Bercovici, 1993, 1995; Tackley, 2000c; Gerya, 2013; Bercovici et al, 2015).

Strain localization is, of course, also observed in nature (e.g. Audet & Bürgmann, 2011; Montesi, 2013; Précigout & Almqvist, 2014) as well as in deformation experiments (e.g. Kohlstedt, 1995; Hansen et al., 2012). In models, strain-localization has been explored for many different processes, including but not limited to, thermal localization (e.g. Schubert & Turcotte, 1972, Thielman & Kaus, 2012; Kiss et al., 2020), damage-dependent weakening (e.g. Tackley, 2000c; Ogawa, 2003; Fuchs & Becker, 2019), power law rheologies (e.g. Jacoby & Schmeling, 1981; King et al., 1992; Weinstein & Olsen, 1992; Bercovici, 1995; Zhong et al., 1998), velocity or pseudo stick-slip weakening (e.g. Bercovici, 1993, 1995), void weakening (e.g. Bercovici & Ricard 2005; Landuyt & Bercovici 2009), or grain-size sensitive rheology in combination with grain-size evolution (e.g. Karato et al., 1980; Kameyama et al., 1997; Braun et al., 1998; Solomatov, 2001; Hieronymus, 2006; Ricard & Bercovici, 2009; Rozel et al., 2011; Bercovici & Ricard, 2012). Overall, strain localization and memory has been shown to be significant for plate boundary formation, e.g. in fault or rift dynamics (e.g. Gerya, 2009; Huismans & Beaumont, 2007; Brune et al., 2014), surface plate motions (e.g. Bercovici and Ricard, 2014; Bercovici et al., 2015), and plate reorganizations (e.g. Wilson, 1966; Sykes, 1878; Gurnis et al., 2001; Audet & Bürgmann, 2011). However, how and to what extent each mechanism contributes to strain localization on lithospheric and mantle scales remains debated (e.g. Montesi, 2013).

In the viscous regime, one important mechanism that has been suggested for localization is grain-size evolution (GSE, e.g. Bercovici and Ricard, 2005; Landuyt and Bercovici, 2009; Bercovici et al., 2015; Foley, 2018). Diffusion creep viscosity is controlled by grain size, and reduction of grain size due to dynamic recrystallization as well as a transition from dislocation creep to diffusion creep dominated deformation can lead to localization (e.g. Braun et al., 1999; Platt & Behr, 2011; Montesi, 2013). However, the physics and formulation of GSE, especially for non-single-phase conditions (such as for a peridotite) and the effects of grain-growth limiting Zener pinning, remain less well constrained (e.g. Bercovici and Ricard, 2016; Mulyukova and Bercovici, 2017, 2018), and grain-size evolution laws remain expensive to implement in large-scale convection models (e.g. Barr and McKinnon, 2007; Dannberg et al., 2017; Foley and Rizo, 2017). Thus, a first order approximation of such microphysical behavior via a parameterized weakening formulation could be helpful.

Damage or “strain” dependent rheologies can possibly provide such a simplification. These are often motivated by dynamic weakening in the brittle/frictional regime where additional weakening mechanisms, such as mineral transformations, serpentinization/mylonitization, partial-melting assisted, flexural/bending weakening, or the coalescence of cracks occur. Such mechanisms can result in a reduction of the effective yield stress (either due to a reduction of cohesion, or reduction of the internal angle of friction) rather than viscosity, as in the case of grain-size evolution. The amount of weakening, for example, governed by mineral transformations in granitic rocks, can be of order of 50-80% (Bos and Spiers, 2002; Huismans and Beaumont, 2007). As a consequence, strain-localization in numerical models for the lithosphere is often modeled by a linear reduction of the yield stress with the accumulated strain (e.g. Lavier et al., 2000; Huismans & Beaumont, 2003; Gerya, 2013; Ruh et al., 2014; Mazzotti & Gueydan, 2018). In those strain dependent weakening (SDW) models, the maximum amount of yield stress reduction is typically assumed to be up to ~ 90%. Different types of SDW have been tested in numerical models (e.g. Huismans & Beaumont, 2003; Gerya, 2013; Brune et al., 2014). With exceptions (e.g. Gerya,2013), one potential issue with many empirical formulations is the lack of a recovery mechanism providing a time scale for a rheological memory, such as would be expected, for example, for the growth of grain-sizes in GSE, or transformation of minerals. This complicates the comparison of damage-dependent implementations to those based on microphysical behavior such as grain-size evolution, and use of SDW models for long-term, thermal convection models.

Given the promise of both GSE and SDW approaches and their respective advantages and drawbacks in terms of physical realism and ease of implementation, we proceed to compare different implementations to highlight their weakening and memory dependent healing behavior using a range of simplified evolutionary deformation tests. We quantify the amplitude and time scales of dynamic weakening and hardening for a pseudo-plastic rheology in combination with "strain"- or damage-dependent weakening (e.g. Tackley, 2000c; Fuchs & Becker, 2019) with a composite rheology (diffusion and dislocation creep; e.g. Hirth & Kohlstedt, 2003) including different grain-size evolutions (e.g. Braun et al., 1999; Behn et al., 2009; Rozel et al., 2011; Dannberg et al., 2017). The SDW formulation is a parameterized, apparent strain weakening method supposed to mimic more complex microphysical localization, weakening and hardening processes, similar but not limited to the effects of GSE.

We conduct a series of numerical, zero-dimensional models assuming a step-like variation in strain-rate over time, or total strain, assuming two different confining conditions, i.e. weakening in the low temperature, brittle regime (e.g. the top of the lithosphere) and weakening in the intermediate temperature, ductile regime (e.g. upper mantle shear zone or lower lithosphere). We consider two different SDW formulations, plastic strain softening (PSS) and viscous strain softening (VSS). The variation in the effective viscosity due to the different GSE models serves as a reference of a microphysical dynamic weakening process to compare with the weakening behavior due to SDW.

Due to the nature of uncertainty of grain-size evolution, we focus on three different GSE models (Braun et al., 1999; Behn et al., 2009; Rozel et al., 2011). Such an exploration of different weakening descriptions can help to better compare different geodynamic models, understand preferred numerical implementations, and contribute to efforts of determining the most appropriate model capturing damage memory in nature.

2 Governing Equations and Modeling Approach

2.1 General Rheology

We focus on weakening and hardening effects in continuous, creeping deformation for pseudo-plastic rheology (e.g. Tackley, 2000; van Heck & Tackley, 2008; Foley & Becker, 2009; Coltice et al., 2017) including strain-dependent weakening (Fuchs & Becker, 2019) and a composite rheology (e.g. Hirth & Kohlstedt, 2003) in combination with grain-size evolution (e.g. Braun et al., 1999; Behn et al., 2009; Rozel et al., 2011; Dannberg et al., 2017), respectively. The governing equations are described in some detail in the following in the hope this helps to clarify their use in the literature. The parameters for each rheology, GSE model, and SDW are also summarized in Table S1 in the supporting information.

2.1.1 Pseudo-Plastic Rheology

A pseudo-plastic rheology, i.e. the combination of a temperature-dependent viscosity and a yield criterion, leads to approximately plate like motions in global, thermal convection models (e.g. van Heck and Tackley, 2008; Foley & Becker, 2009; Coltice et al., 2017). The temperature-dependent viscosity can be described, for example, by an Arrhenius-type viscosity (e.g. Tackley, 2000b, c):

$$\eta_T = \eta_0 \exp\left[\eta_1\left(\frac{1}{T+1}-\frac{1}{2}\right)\right] \tag{1}$$

where T is the non-dimensional temperature, η_0 a pre-exponential factor (here unity due to non-dimensionalization) and η_1 is the non-dimensional activation energy.

The yield and effective viscosity, η_y and η_{eff}, for a pseudo-plastic rheology can be defined as (e.g. Tackley, 2000b, c):

$$\eta_y = \frac{\sigma_y}{2\dot{\varepsilon}_{II}}, \tag{2}$$

$$\eta_{eff} = \min\left(\eta_T, \eta_y\right), \tag{3}$$

where σ_y is the yield stress (either depth-dependent or constant, depending on assumptions) and $\dot{\varepsilon}_{II}$ is the second invariant of the strain-rate tensor. While rock strength will depend on different parameters (e.g. temperature, pressure, volatile content, composition; e.g. Kohlstedt et al., 1995), we assume a fixed, initial yield stress σ_y as the “undeformed” condition at a certain temperature and strain rate. Depending on the SDW regime we assume to be active, i.e. plastic (PSS)- or viscous (VSS)-strain softening (see below), the initial yield stress is assumed to be either small enough to enable yielding within the defined strain-rate range (PSS) or large enough to avoid yielding (VSS).

2.1.2 Composite Rheology

Assuming a constant strain rate the viscosity for each deformation mechanism of a composite (diffusion and dislocation creep) rheology and the effective viscosity can be defined by (e.g. Hirth & Kohlstedt, 2003):

$$\eta_i = \frac{1}{2} A_{i,0}^{-\frac{1}{n_i}} \mathcal{R}^{m_i} \exp\left(\frac{Q_i}{n_i RT}\right) \dot{\varepsilon}_{i,II}^{\frac{1}{n_i}-1}, \tag{4}$$

$$\eta_{eff} = \left(\frac{1}{\eta_l}+\frac{1}{\eta_f}\right)^{-1}, \tag{5}$$

where A_0, n, m, $\mathcal{R}$, Q_i, R, T, $\dot{\varepsilon}_{i,II}$ are the pre-exponential factor (including the conversion to use the strain rate second invariant), the power-law exponent, the grain-size exponent, the grain size, the activation energy, the gas constant, the absolute temperature, and the strain rate for each deformation mechanism, respectively. The index i stands for the different deformation mechanisms, i.e. dislocation (l) and diffusion (f) creep (see supporting information S2).

Below, to simplify the analysis, we focus on a temperature and strain-rate range in which diffusion creep dominates; hence the effective viscosity is mainly governed by diffusion creep.

2.2 Strain-Dependent Weakening (SDW)

Different localization mechanisms have different potential for weakening (e.g. Montési, 2013) and their relevance for different parts of the Earth remains debated. Here, we use a description of weakening due to a general damage formulation depending on the accumulated apparent strain γ (Fuchs & Becker, 2019). This "strain" γ is not the real strain (which cannot be removed, for example) nor a proper state variable, but rather an apparent, strain-dependent damage control parameter including a temperature-dependent healing component. For the sake of convenience, we will refer to this apparent strain variable γ as "strain" in the following.

The temporal evolution of the strain is defined by (e.g. Tackley, 2000c; Gerya, 2013; Fuchs & Becker, 2019):

$$\frac{d\gamma}{dt} = \dot{\varepsilon}_{II} - \gamma H(T), \tag{6}$$

where γ is the apparent strain, $\dot{\varepsilon}_{II}$ the second invariant of the strain-rate tensor, T the temperature, and H the temperature-dependent healing rate defined by:

$$H(T) = B\exp\left[-\frac{\eta_2}{2}\left(\frac{1}{T+1}-\frac{1}{2}\right)\right], \tag{7}$$

where B is the healing time scale and η_2 a non-dimensional temperature activation constant, i.e. for a high (low) η_2 the healing term depends more (less) on temperature. Fast healing is always focused within high temperature ranges, but for high η_2 the healing effect is almost negligible for lower temperatures (e.g. Fuchs & Becker, 2019).

The temperature-dependent healing rate is assumed to be an average of a possibly constant and purely temperature-dependent healing rate (e.g. due to diffusion processes), which can be described by half the inverse of the diffusion creep viscosity (e.g., Tackley, 2000b). Temperature-dependent healing avoids infinite strain accumulation and leads to long-term strain memory in the cold lithosphere and removal of damage within the hotter asthenosphere. The apparent strain hardening mechanism mimics a reduction of the effective strain either by mixing and stirring of the mantle with typical strain rates of the mantle or due to temperature-dependent microphysical processes (e.g. diffusion or grain growth). For SDW, we always assume the strain rate of eq. (6) to be the total strain rate. To allow for maximum weakening to be uniquely described by the critical strain and maximum damage, and to avoid a time lag of strain hardening once deformation ceases, we assume that no further damage accumulates once the critical strain is reached. Thus, we assure that strain hardening initiates at the same time grain growth initiates. The amplitude of weakening/hardening in the composite, grain-size sensitive rheology, is then determined by the strain-weakening parameters, which control the rate and amplitude of the strain weakening.

The amount of the "damage" $\mathcal{D}$ is assumed to depend linearly on the accumulated strain γ (e.g. Lavier et al., 2000; Huismans & Beaumont, 2003; Gerya, 2013; Mazzotti & Gueydan, 2018):

$$\mathcal{D} = \mathcal{D}_{\max} \frac{\gamma(t)}{\gamma_{cr}}, \tag{8}$$

where $\mathcal{D}_{\max}$ is the maximum damage (here 90%), $\gamma(t)$ the strain at time t, and γ_{cr} the critical strain to reach maximum weakening. Following this parameterization of SDW (Fuchs & Becker, 2019), $\mathcal{D}$ is mainly controlled by two factors: a) the critical strain γ_{cr} and b) the healing rate H, which is governed by the temperature T, the healing time scale B, and the temperature activation term η_2.

Assuming constant total strain rate, the two competing mechanisms of weakening and healing lead to a steady-state condition of damage after a certain period, similar to a steady-state grain size (see supporting information eqs. S7-S8). The maximum steady-state damage decreases with an increasing critical strain γ_{cr} and healing time scale B. Damage reduction is governed by the healing rate H. For example, assuming deformation is not active, i.e. strain rate is equal to zero, eq. (6) leads to an exponential decay. The time to reduce the accumulated "strain" is inversely proportional to the healing rate H (see supporting information eq. S9). Figure 1 shows that the range of healing time scales used in this study does overall match the time scales expected for grain growth.

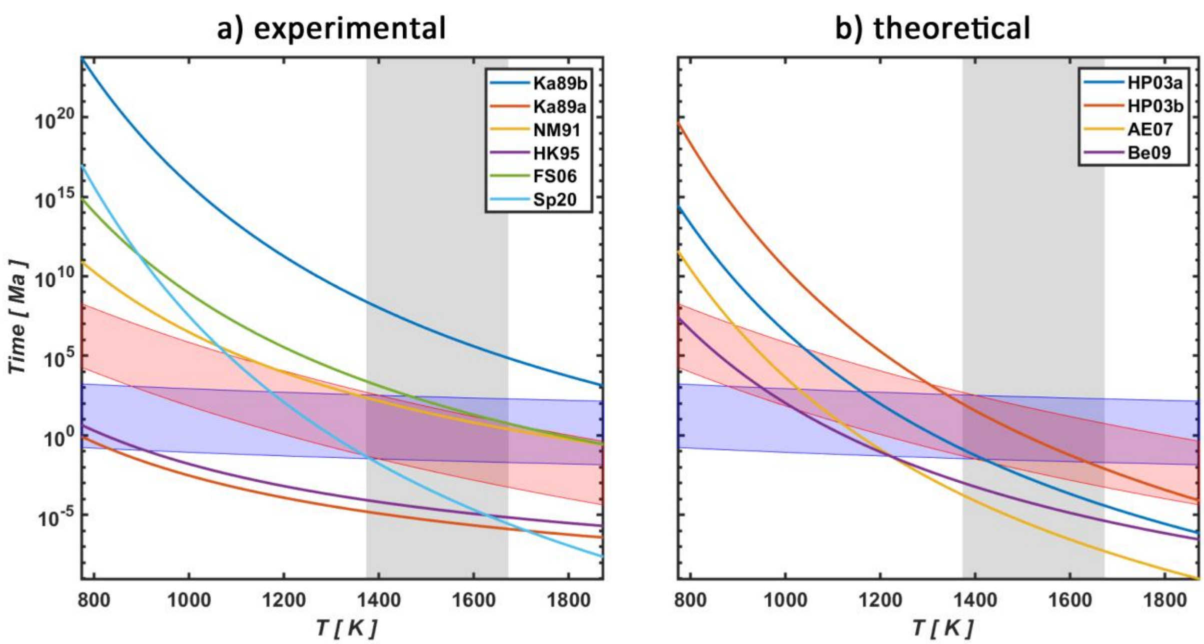

Figure 1. Grain-growth times t_{ge} (in Ma) needed to increase an initial grain size (1 mm) by a factor of e using different a) 'experimentally' and b) 'theoretically' calibrated grain-growth data (k_0, Q_G, and p). The growth time is calculated following supporting information eq. (S13). The gray (vertical) shaded area shows the temperature range used in grain-growth experiments (Ka89b: "dry" Karato, 1989; Ka89a: "wet" Karato, 1989; NM91: Nichols & Mackwell, 1991; HK95: Hirth & Kohlstedt, 1995; FS06: Faul & Scott, 2006; Sp20: Speciale et al., 2020; HP03a: Hall & Parmentier, 2003; HP03b: Hall & Parmentier, 2003; AE07: Austin & Evans, 2007; Be09: Behn et al., 2009). The colored shaded areas show the range of apparent-strain reduction time (by a factor of $1/e$), calculated by supporting information eq. (S9), for a certain range of healing time scales B (dimensional: $10^{-16} - 10^{-12}$ s^{-1}; scaled: $10^{-2} - 10^{2}$) and different thermal activation constant η_2 (blue: 23.03; red: 184.21).

How deformation leads to weakening and localization within the lithosphere remains unclear, but lithospheric strain weakening is a commonly used mechanism in geodynamic models. Different versions of strain weakening have been used in thermal convection modeling (e.g., Tackley, 2000b; Ogawa, 2003; Gerya, 2013; Fuchs & Becker, 2019) and lithospheric deformation models (e.g. Lavier et al., 2000; Huismans & Beaumont, 2003; Brune et al., 2014; Ruh et al., 2014; Mazzotti & Gueydan, 2018). We focus on the lithospheric mechanical approach and seek to combine it with a more realistic hardening component.

Strain-dependent weakening within the lithosphere for a pseudo-plastic rheology may work differently depending on the rheological element where weakening is active (e.g. Huismans & Beaumont, 2003). Weakening is often described by a linear decrease of the yield stress (plastic(-strain) softening, PSS), or by a (linear) decrease of the viscosity (viscous(-strain) softening, VSS), as a function of total viscous strain γ_{tot} or plastic strain $\gamma_{plastic}$ (more precisely the integral of the second invariant of corresponding strain-rate tensor). In case of PSS, one assumes weakening is applied due to a reduction of the yield stress (or yield viscosity in numerical implementations), e.g. due to change in pore fluid pressure, due to fault gouge formation, mineral transformation, or serpentinization and mylonitization. In case of VSS, one assumes weakening is applied due to a reduction of the temperature-dependent, or diffusion creep viscosity, approximating the weakening effects from e.g. grain-size reduction due to dynamic recrystallization or other effects.

To test different weakening descriptions for SDW, we use three different formulations:

$$\tilde{\eta}_{eff} = \begin{cases} \min\left(\eta_T, \tilde{\eta}_y\right); \text{ with } \tilde{\eta}_y = \eta_y\left(1-\boldsymbol{\mathcal{D}}\right) \\ \min\left(\tilde{\eta}_T, \eta_y\right); \text{ with } \tilde{\eta}_T = \eta_T\left(1-\boldsymbol{\mathcal{D}}\right), \\ \min(\eta_T, \eta_y)\cdot\left(1-\boldsymbol{\mathcal{D}}\right)^q \end{cases} \tag{9}$$

where the first mechanism (SDW-I) assumes weakening only within the plastic regime (i.e. PSS), the second (SDW-II) assumes weakening only within the viscous regime (i.e. VSS), and the third (SDW-III) assumes weakening occurs in both regimes but with a power law according to q (similar to a grain-size sensitive diffusion creep rheology; see sec. 2.1.2). For q = 1, SDW-III is a combination of the first two. We assume that deformation takes place entirely in the plastic regime for SDW-I (equal to only using the plastic component of strain), and in the viscous regime for SDW-II and SDW-III to avoid weakening due to the change in strain rate, i.e. the yield stress is high enough to avoid yielding.

2.3 Grain-Size Evolution (GSE)

Grain size affects the effective viscosity and the transition between deformation mechanisms due to grain-size sensitive diffusion creep and grain-size reduction in dislocation creep (e.g. Twiss, 1977; de Bresser et al., 1998). Although the differences in the steady-state grain size as well as in the effective viscosity are only minor for different grain-size evolution formulations (Figure 2), the influence on the dominant deformation mechanism at different steady-state confining conditions (i.e. T and ε_{II}, see Figure 2) might still be important, for example in terms of controlling the distribution of seismic anisotropy in the upper mantle (e.g. Becker et al., 2008; Behn et al., 2009) or strain localization processes in ductile shear zones due to dynamic recrystallization (assuming grain-size reduction is only governed by dislocation creep).

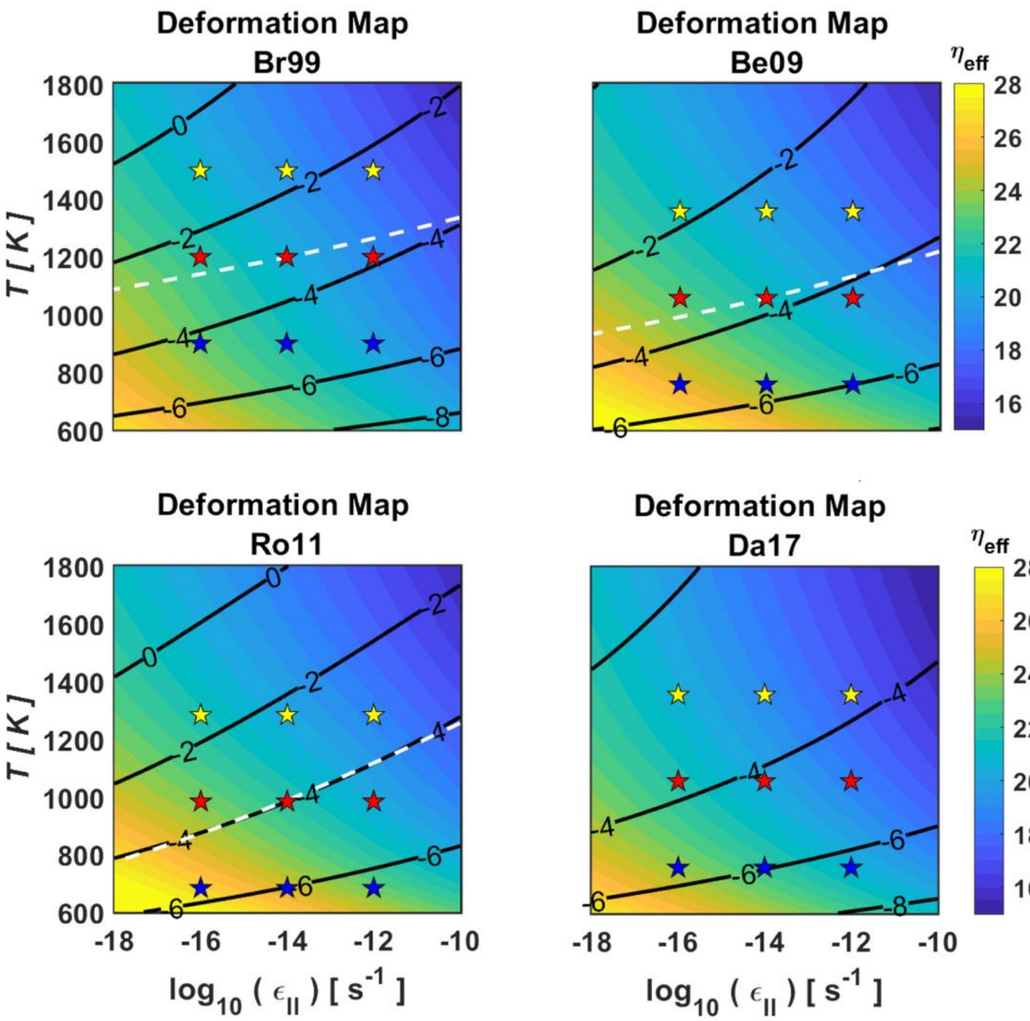

Figure 2. Deformation map for composite, grain-size sensitive rheologies (assuming different steady-state grain sizes; see supporting information S4). Effective viscosity η_{eff} (background color scale in Pa·s) in the temperature T and total strain rate $\dot{\varepsilon}_{II}$ parameter space using dry olivine, composite (diffusion and dislocation creep) rheology parameters from Hirth and Kohlstedt (2003) and assuming a steady-state grain size (solid, numbered lines; $\log_{10}(\mathcal{R}_{eq})$ in m) for different grain size evolution (GSE) models (Br99: Braun et al. (1999) without implicit grain growth; Be09: Behn et al., 2009; Ro11: Rozel et al., 2011; Da17: Dannberg et al., 2017). The white dashed contour line is the transition between dislocation (high T and large $\mathcal{R}$) and diffusion (low T and small $\mathcal{R}$) creep dominated deformation mechanism (lies outside the T and $\dot{\varepsilon}_{II}$ range for Da17). The star symbols in each plot are the temperatures (low, intermediate, and high) and strain-rate ranges used in the step-like deformation calculations for different GSE- and strain-dependent weakening models.

To better understand the temporal evolution of each GSE-model, we analyzed the dynamics of grain growth and reduction, assuming only one mechanism is active. Steady-state grain sizes tend to reach large values for high temperatures and low strain rates. This is mainly due to the assumption of a single-mineral phase. Assuming the presence of secondary phases, impurities, or partial melt would significantly limit the growth rate and the maximum grain-size (e.g. Nichols & Mackwell, 1991; Faul & Scott, 2006; Faul & Jackson, 2007; Hiraga et al., 2010;

Bercovici & Ricard, 2014; Dannberg et al., 2017). For the sake of simplicity, however, we only focus on single-phase GSE-models but include one model with slower grain-growth (i.e. Dannberg et al., 2017).

The evolution of a volumetric averaged grain size of a rock is assumed to be governed by competing grain growth (e.g. Hillert, 1965; Karato, 1989; Evans et al., 2001) and grain-size reduction due to deformation (e.g. Twiss, 1977; Ricard & Bercovici, 2009), here mainly expressed by dynamic recrystallization (e.g. Karato, 1989; de Bresser et al., 1998; Austin & Evans, 2007; Rozel et al., 2011). Grain reduction is thus controlled by the amount of dislocation creep and grain-size variation is assumed to be driven by the change of the total grain boundary energy (increase for grain-size reduction and decrease for grain growth). In general, both processes are controlled by two macroscopic parameters (i.e. temperature T and deformational work $\psi = \tau \cdot \dot{\varepsilon}$). Assuming both processes occur simultaneously, the overall rate for GSE can be written as a sum of growth and reduction rates:

$$\frac{d\mathcal{R}}{dt} = \frac{d\mathcal{R}_{grwoth}}{dt} + \frac{d\mathcal{R}_{reduction}}{dt}, \tag{10}$$

i.e. steady-state implies a balance of grain growth and reduction.

2.3.1 Grain-Size Coarsening

Grain-size coarsening is governed by the reduction of grain boundary energies due to grain boundary migration (e.g. Karato, 1989; Evans et al., 2001) and most likely to be active in both dislocation and diffusion creep. The most common mechanism for grain growth of olivine is assumed to be thermally activated normal or static grain growth (e.g. Urai et al., 1986; Karato, 1989). Grain-growth kinetics are well known (Hillert, 1965; Atkinson, 1988) and material constants for different environments (e.g. temperature, confining pressure, etc.) have been calibrated for olivine (e.g. Karato, 1989; Nichols & Mackwell, 1991; Hirth & Kohlstedt, 1995; Faul & Scott, 2006; Hiraga et al., 2010) and other minerals (e.g. Austin & Evans, 2007, and references therein). The growth rate can be written as (e.g. Montési & Hirth, 2003):

$$\frac{d\mathcal{R}_{growth}}{dt} = \mathcal{C}_g \mathcal{R}^{1-p}, \tag{11}$$

where $\mathcal{C}_g$ is a temperature and material dependent rate constant (see supporting information S4).

The growth rate constant $\mathcal{C}_g$, as defined in eq. (11), is controlled mainly by temperature but also pressure, water content, and impurities (e.g. porosity, melt content, and secondary phases). In addition, a calibration assuming a different GSE-model (e.g., as a piezometer; e.g. Karato, 1989; de Bresser et al., 1998; or as a wattmeter; e.g., Austin & Evans, 2007; Behn et al., 2009) leads to different grain-growth constants, although the resulting large values for p (~ 4) remain debated (see supporting information S4; e.g. Bercovici & Ricard, 2013, 2014). The different calibrations that are currently in use, in fact, lead to huge variations in the relative growth time t_{ge} (Figure 1).

Two major differences are inherent in Figure 1. First, the growth time increases significantly due to impurities in the sample. The parameters of Ka89a and HK95 (see caption) have the smallest growth time over a wide temperature range, mainly due to a single mineral phase system. Second, the slope of the growth rate with temperature differs as well, indicating an increased dependence on temperature (i.e. high activation energy > 500 kJ/mol). Most grain-growth experiments are constrained to a limited temperature range (~1100-1400 °C) or confining pressures (~ 10^{-1}-10^{3} MPa) and extrapolation is always subject to uncertainties. Further experiments on grain growth might significantly reduce such ambiguities.

2.3.2 Grain-Size Reduction

Grain-size reduction can be governed by different mechanisms (e.g., Twiss, 1977; Karato, 1980; van der Wal et al., 1993; Austin & Evans, 2007; Ricard & Bercovici, 2009; Rozel et al., 2011). We focus on grain-size reduction due to dynamic recrystallization, which occurs mainly during deformation in which the total grain-boundary energy increases, i.e. grain sizes are reduced by a fraction of the deformational work in the dislocation creep regime which results in an increase of the internal energy.

An early exploration of a GSE-model (e.g. Twiss, 1977; Karato, 1980) found that the steady-state grain-size is related to the applied stress. This stress – grain-size relationship is called the piezometric approximation (or (paleo)piezometer when applied to actual rock textures). Assuming grain size approaches the piezometer and the internal grain-boundary energy increases due to dynamic recrystallization, a simple grain-size evolution model has been developed (see supporting information S4; e.g. Kameyama et al., 1997; Braun et al., 1999):

$$\frac{d\mathcal{R}_{reduction}}{dt} = -\mathcal{C}_{r,1}\dot{\varepsilon}_{II}\left(\mathcal{R} - \mathcal{R}_{\infty}\right), \tag{12}$$

where $\mathcal{C}_{r,1}$ is a grain-size reduction rate constant and $\mathcal{R}_{\infty}$ is the piezometric value proportional to the applied stress.

Another GSE-model postulates that the reduction of grains is driven by the rate of deformational work (e.g. Austin & Evans, 2007; Behn et al., 2009). This model has been extended into a thermodynamically, self-consistent model including a temperature sensitive work partitioning and log-normal distribution of grain sizes (e.g. Ricard & Bercovici, 2009; Rozel et al., 2011). In both approaches, grain-size reduction is driven by the rate of work, i.e. the rate of change of internal energy plus the rate of energy dissipation (e.g. Austin & Evans, 2007). The rate of grain-size reduction for both models can be simplified to:

$$\frac{d\mathcal{R}_{redcution}}{dt} = -\mathcal{C}_{r,2/3}\tau_{II}\dot{\varepsilon}_{II,l}\mathcal{R}^{2}, \tag{13}$$

where $\mathcal{C}_{r,2/3}$ are the grain-size reduction rate constants depending on the assumed model for grain-size reduction (e.g. Br99: Braun et al., 1999; AE07: Austin and Evans, 2007; Be09: Behn et al., 2009; Ro11: Rozel et al., 2011; Dan17: Dannberg et al., 2017), which are governed by the specific grain-boundary energy, geometrical constants, grain-size distribution, or work partitioning (see supporting information S4). Steady state for those two models does not depend on the stress alone, but on the deformational work from dislocation creep $\psi_l = \tau \cdot \dot{\varepsilon}_l$. This is called the wattmeter (e.g. Austin & Evans, 2007).

Assuming a constant work ($\psi = \tau_{II} \cdot \dot{\varepsilon}_{II}$), temperature, and no grain growth, we can calculate the relative grain-size reduction time t_{re} for different GSE-models (Figure 3), i.e. the time required to decrease a certain grain size at a certain ψ and T by a factor of $1/e$ (see supporting information S4). The shaded areas of Figure 3 show the range of t_{re} between 1-10 Ma, i.e. grain-size reduction is fast for high ψ and slow for low ψ and, depending on the model, fast at high T. Assuming grain-size reduction is governed by dislocation creep only (b, c, d, e), one obtains different reduction rates depending on the partitioning between dislocation and diffusion creep. Including a temperature-dependent partitioning of the deformational work (d), the reduction rate decreases again with increasing temperature, as more of the deformational work is partitioned into viscous dissipation than into the reduction of grain size.

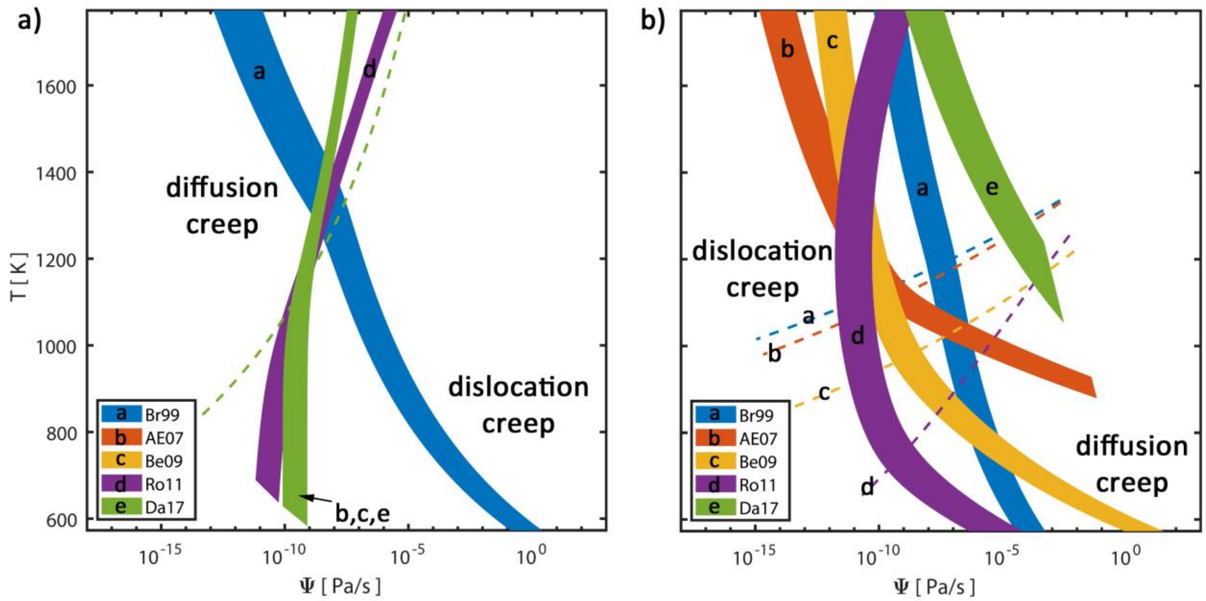

Figure 3. Grain-size reduction time t_{re} (right of each shaded areas – less than 1 Ma; left of shaded areas: more than 10 Ma) to reduce a constant grain size of 1 mm (a) or the steady-state grain size at a certain total deformational work ψ (= $\dot{\varepsilon}_{II} \cdot \tau_{II}$) and temperature T (b) by a factor of 1/e, assuming a constant ψ and T, using different grain-size evolution (GSE) models assuming only grain-size reduction is active (Br99: Braun et al., 1999; AE07: Austin & Evans, 2007; Be09: Behn et al., 2009; Ro11: Rozel et al. 2011; Da17: Dannberg et al., 2017). The reduction time is from eqs. (S21) and (S22). The stress and steady-state grain size for a constant total strain rate $\dot{\varepsilon}_{II}$ and temperature T are calculated iteratively using the rheological parameters of Hirth and Kohlstedt (2003) for a composite (diffusion and dislocation creep), dry olivine rheology. The colors and lower-case letters indicate each GSE-model, where the dashed lines are the transition from dislocation to diffusion creep, respectively.

Assuming a constant grain size ($\mathcal{R}$ = 1 mm) removes the rheological effect (Figure 3a), as the stress and effective viscosity remain the same for each GSE-model, and the relative reduction time is only governed by the reduction rate constant as defined for each GSE-model ($\mathcal{C}_{r,1/2/3}$), i.e. assuming a piezometer, wattmeter, or the thermodynamically self-consistent model. The thermodynamically self-consistent model and the wattmeter yield similar results, whereas the piezometer differs significantly (since one uses the total strain rate in this model). The relative reduction time for an initial steady-state grain size (Figure 3b) shows how the reduction rate is controlled by the partitioning between dislocation and diffusion creep deformation, which is governed by the actual grain size at that temperature and total deformational work (i.e. slow for large $\mathcal{R}$ and small ψ and fast for small $\mathcal{R}$ and high ψ). This comparison shows that grain-size reduction is significantly faster (Figure 3a and 4) assuming GSE-models based on the wattmeter approximation (AE07, Be09, Da17) or the thermodynamically self-consistent model (Ro11) compared to the piezometer approximation (Br99).

2.4 Modeling Approach

To analyze the effects of damage evolution in a pseudo-plastic rheology including SDW and a composite rheology including GSE, we conducted a series of numerical, zero-dimensional, experiments assuming a step-like variation of the total strain rate $\dot{\varepsilon}_{II}$ (e.g. 10^{-14}, 10^{-12}, 10^{-16}, 10^{-14} s^{-1}) akin to rate-state frictional sliding tests. We found both non-dimensionalized and dimensional views of the results instructive, and therefore show results where "experiments" run over stages with a fixed time, t (0.1553 Ma), or stages with a fixed total strain ($\gamma_{tot} = 1.25$; i.e. the time integral over the total strain-rate). The total duration in experiments with constant time (0.621 Ma) was chosen to yield a cumulative strain of 5 similar to the maximum total strain accumulated in the constant strain case (see small plots on the side of Figures 4-6).

To model GSE, we integrate eq. (10) forward in time assuming constant stress and temperature using the MATLAB solver for ordinary differential equations (ODE, *ode45*). Care has to be taken to use a small enough tolerance for the GSE models with a fast healing rate (Ro11) at low temperatures to ensure a stable solution. At each time step, we iteratively solve eqs. (4) and (5) for the dislocation and diffusion creep strain rates (up to 30 iterations, using 50% of the new solution only for damping), assuming a constant grain size, temperature, and total strain rate, until the viscosity for each deformation mechanism remains constant (< 0.1 % variation). We solve the equations for composite rheology including GSE (eqs. 10-13) using the rheological parameters for a composite, dry olivine rheology from Hirth and Kohlstedt (2003) and four different GSE-models (i.e. Br99, Be09, Ro11, and Dan17) at three different constant temperature conditions (low, 700-900 °C, intermediate, 1000-1200 °C, and high, 1300-1500 °C; see Figure 2; for more details see supporting information S2-S4). We assume that the strain rate for grain-size reduction is the dislocation creep part of the total strain rate, if not stated otherwise.

The initial temperature and grain size are defined by the steady-state condition for a total strain rate of 10^{-14} s^{-1} at the transition between dislocation and diffusion creep for each GSE-model (see middle red star in Figure 2), except for Dan17 in which the transition lies outside the strain-rate/temperatures considered and the same initial temperature condition as for Be09 was used. Steady state conditions are used as initial condition to obtain a stable solution. For the given initial strain rate (10^{-14} s^{-1}) and temperatures (low, intermediate, and high), grain size quickly reaches steady-state for a wide range of initial grain sizes (from 1 μm up to 1 cm; except for the low temperature and 1 μm case).

For the pseudo-plastic rheology including SDW, we calculate the apparent strain γ (eq. 6-9) using the same ODE solver and a range of critical strains γ_{cr} (1, 5, 10) and healing time scales B (10^{-16}, 10^{-14}, 10^{-12} s^{-1}). The accumulated strain $\gamma(t)$ defines the amount of damage (eq. 8), and hence weakening (eq. 9). We used SDW-I, SDW-II, and SDW-III, as defined above, to analyze damage evolution. The apparent strain from eq. (6) is not the same as the total actual strain γ_{tot} (Figure 5), which is defined by the time integral of the second invariant of the total strain rate.

We show the temporal evolution of grain size, diffusion creep viscosity, deviatoric stress, and logarithm of the ratio of the dislocation and diffusion creep strain rates for each GSE-model, before comparing the weakening and hardening effects of different weakening mechanisms.

Only intermediate temperature ranges are shown as those are where diffusion creep dominates at the applied strain rates (see Figures 2 and 4). Intermediate temperatures present an upper limit for dynamic weakening due to GSE. Considering GSE governs the diffusion creep, this intermediate temperature range most likely represents the deepest lithospheric conditions in which visco-plastic strain softening will be significant.

3 Results

3.1 GSE in consecutive deformation

Steady-state grain sizes are governed by temperature, strain rate, stress, and the growth and reduction rate of each GSE model (Figure 4). The absolute temperatures for the range explored for each model are not equal (cf. Figure 2), which leads to additional variations in effective viscosity, even in cases with similar grain size. However, the variation of the diffusion creep viscosity is only governed by the growth and reduction rate of each GSE model, and thus the variations during grain growth and reduction, respectively. The stress varies according to the instant changes in the acting total strain rate and thus the strong stress peaks at the beginning of each stage, followed by a relatively smooth transition towards steady-state (due to grain-size reduction or growth).

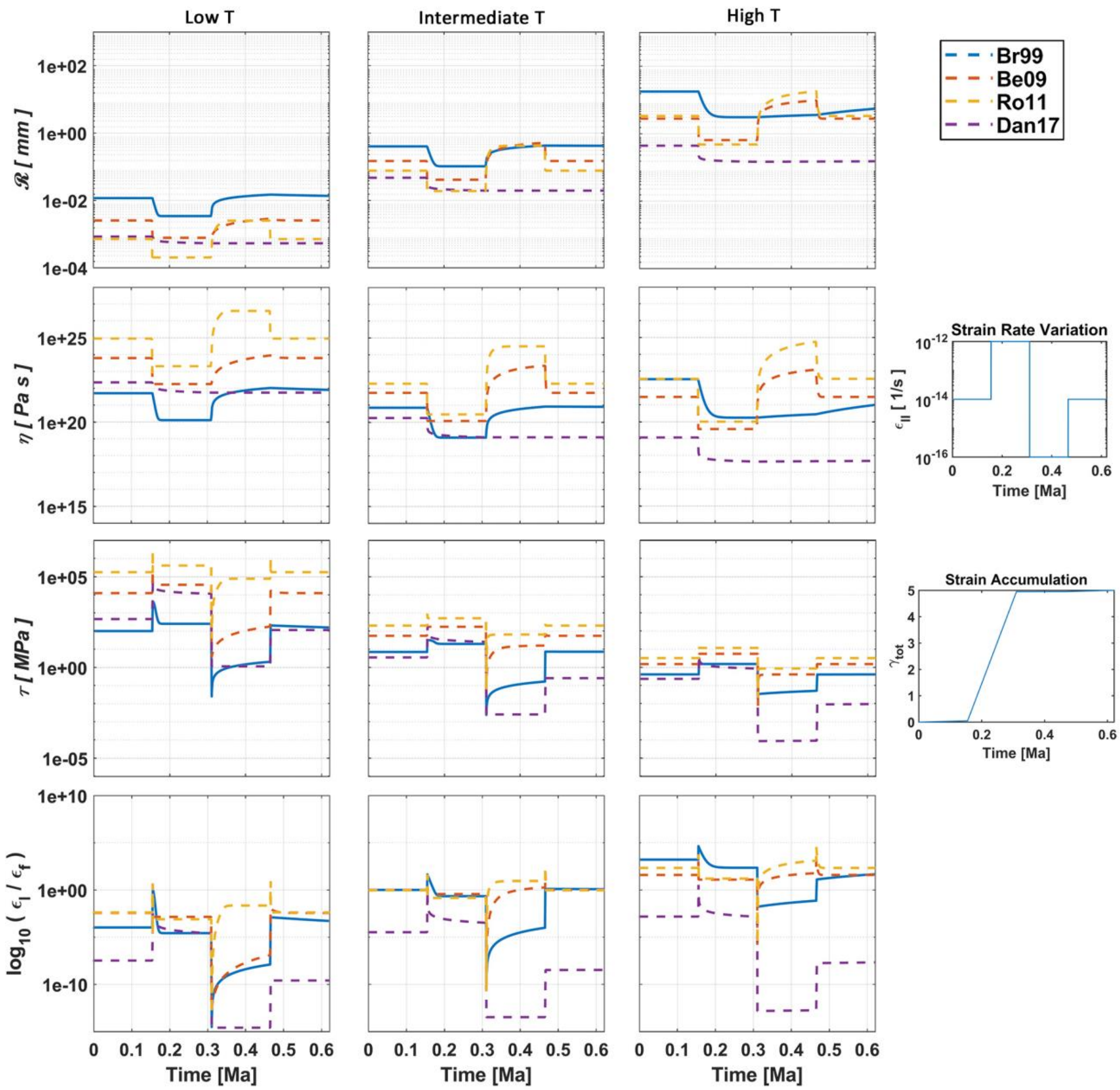

Figure 4. Variation of the grain size $\mathcal{R}$ (in mm), the diffusion creep viscosity η_f (in Pa·s), the shear stress τ (in MPa), and the logarithm of the dislocation-diffusion creep strain-rate ratio with time for four different grain size evolution (GSE) models (Br99: Braun et al., 1999; Be09: Behn et al, 2009; Ro11: Rozel et al., 2011; Dan17: Dannberg et al., 2017) and three different temperature conditions (low, intermediate, and high). Initial steady-state grain size, temperature, and strain rate for each GSE-model are defined by the middle column of stars in Figure 2. The total strain rate $\dot{\varepsilon}_{II}$ varies step-like in four stages as 1, 100, 0.01, 1 times 10^{-14} s^{-1}, and remains constant over equally long periods of 0.1553 Ma (non-dimensional 0.049). The maximum time 0.6213 Ma (0.1961) is given by the time required to accumulate a total shear strain of 5, i.e. the integral of the total strain rate $\dot{\varepsilon}_{II}$ over time. The smaller plots on the right show the variation of the total strain rate and the total strain γ_{tot} with time.

For each temperature range, the transient behavior varies significantly between the different models resulting in different viscosity variations. The strongest difference is observable for Dan17 due to a significantly slower growth rate compared to Br99, Be09, or Ro11. A reduction of grain size is seen at the first strain rate increase at every temperature, but grain growth is negligible, even for the high temperature case.

In the following, we will focus on the differences between Br99, Be09, and Ro11. These models are most similar at the intermediate temperature range (middle column in Figure 4). All models show a grain-size reduction due to the increase of the total strain rate and growth governed by the actual grain size and temperature (eqs. 11-13), except at the beginning of the last stage of Br99. This is artificial, however, since the grains reach a size during grain growth in the third stage similar to the steady-state grain size of the last stage. This shows a significant difference between the GSE rates for the piezometer and the remaining models (cf. the diffusion creep regime in Figure 3). Only minor differences are observable in grain-size reduction between the wattmeter (Be09) and the thermodynamically self-consistent model (Ro11), both of which adjust much faster than the piezometer (Br99). Regarding the growth rate, Ro11 is much faster than Be09 and always reaches steady-state. This is even more pronounced at low temperatures (due to the already small grains).

At the low temperature range (left column in Figure 4), viscosity and thus stress reaches a maximum. Therefore, we obtain the smallest steady-state initial grain size (see supporting information eqs. S24-S26), which also affects the growth rate (eq. 11). The combination of a smaller steady-state grain size and a smaller growth rate (especially for Be09 and Ro11) results in an overall smaller variation of the grain size. The smaller absolute and steady-state grain size also favors a faster grain ‘growth’ for the piezometer (see eq. 12 and supporting information eqs. S14-S16). However, grain growth in the low temperature range is significantly only for Ro11. Steady-state grain size is never reached in the growth phase for the remaining GSE-models. While grain growth remains faster for Br99 in comparison to Be09, grain-size reduction remains smaller.

Overall, the most time-dependent GSE model is the piezometer (Br99) with the slowest reduction and growth rate (besides Dan17). The wattmeter (Be09) has a much faster reduction rate, but still a slower growth rate than the thermodynamically self-consistent model (Ro11), especially at low temperatures. Ro11 is thus the least time-dependent model, and reaches steady-state extremely fast, especially for grain reduction which happens almost instantly. Considering the significantly different timescales of grain growth depending on the conditions, however, this could change using more realistic assumptions (e.g. assuming two mineral phases), which would decrease the growth rate (as for Dan17). A slower growth rate would more likely ensure the preservation of weak zones and tectonic inheritance especially in the low temperature regimes. It is thus important to consider which GSE model might best approximate the processes that are to be explored geodynamically.

Grain-size evolution and the viscosity in the high temperature ranges are shown here only for the sake of completeness. Since most deformation takes place in dislocation creep, the effective viscosity is no longer governed by GSE (not shown here), which prevents any dynamical weakening or hardening effect due to GSE. The steady-state grain size for each GSE model is larger (up to 20 mm for the piezometer) in comparison to the colder temperature ranges, which reduces the growth rate (steady-state is not reached in the growth phase for any of the GSE models). At the beginning of the third stage, however, grain growth remains relatively fast and the grains approach almost steady-state (except for Br99 due to the already large grains). Therefore, even smaller grains, to force the material into diffusion creep, would rather grow fast and deformation would instantly transition back into dislocation creep. Interestingly, a strain-rate increase by two orders of magnitude ($10^{-14} – 10^{-12}$ s^{-1}) is not sufficient to transition into diffusion creep (except for Da17 which already lies in diffusion creep). Due to the high temperatures, the effective viscosity would also be rather small, potentially preventing any viscous shear localization for typical geological strain rates (~$10^{-14} – 10^{-15}$ s^{-1}).

Except for the piezometer, grain-size reduction thus leads to fast rheological weakening with viscosity reduction of around two orders of magnitude. Hardening also occurs relatively fast but varies significantly between the GSE models, especially in the low temperature range, with a viscosity between two (Br99 and Be09) and four (Ro11) orders of magnitude. We next focus on the variation of the diffusion creep viscosity within the intermediate temperature ranges and compare their transient behavior with a pseudo-plastic rheology including SDW.

3.2 Comparison of SDW and GSE Models for Intermediate Temperature Deformation

We compare three different SDW mechanisms with the GSE-models (Figures 5 and 6). The effective viscosity of the pseudo-plastic rheology including SDW is shown along with the diffusion creep viscosity for each GSE model (dashed, black lines). The colored shaded area is the range of the visco-plastic viscosity including strain-dependent weakening for different healing time scales B (scaled by the reference strain rate $\dot{\varepsilon}_{sc} = 10^{-14}$ s^{-1}; i.e. blue: 10^{-2}: red: 1, yellow: 10^{2}) and different critical strains γ_{cr} (dashed lines: 1, solid lines: 5, dash-dotted lines: 10). Each row shows the weakening and hardening effects due to one SDW mechanism in comparison to the grain-size evolution of the three different GSE-models. The small plots on the right side show the variation of the strain rate (Figure 5) over time (or the total strain γ_{tot} in Figure 6) and the corresponding accumulated total strain γ_{tot} (or the required non-dimensional time in Figure 6). A summary of the weakening and hardening effects of the different SDW mechanism and their resemblance with GSE is given in the Table below.

Table 1

Summary of Weakening and Hardening Effects for SDW, where $\mathcal{O}$ indicates order of magnitude for the viscosity reduction, which is ~ $\mathcal{O}(100)$ for GSE

Weakening Mechanism	Weakening Effect	Hardening Effect
SDW-I (PSS)	Fast for $\gamma_{cr} < 5$ Somewhat more effective ($\mathcal{O}(1{,}000)$)	Slow for $B \leq 1$ Akin to GSE for $B = 100$ and $\gamma_{cr} = 1$
SDW-II (VSS)[a]	Fast for $\gamma_{cr} < 5$ Less effective ($\mathcal{O}(10)$) than GSE	Clear hardening effect only for $B = 100$ Less effective and slower than GSE
SDW-III (VSS)[a]	Fast for $\gamma_{cr} < 5$ Somewhat more effective ($\mathcal{O}(1{,}000)$)	Clear hardening effect only for $B = 100$ Slower than GSE

Note. [a]Do not fully resemble the transient behavior of GSE.

3.2.1 Plastic Strain Softening

For SDW-I, we assume deformation only takes place in the plastic regime, eq. (9), where damage leads to a linear reduction of the yield stress or yield viscosity (top row in Figure 5). Thus, the pseudo-plastic viscosity instantly changes with the strain rate.

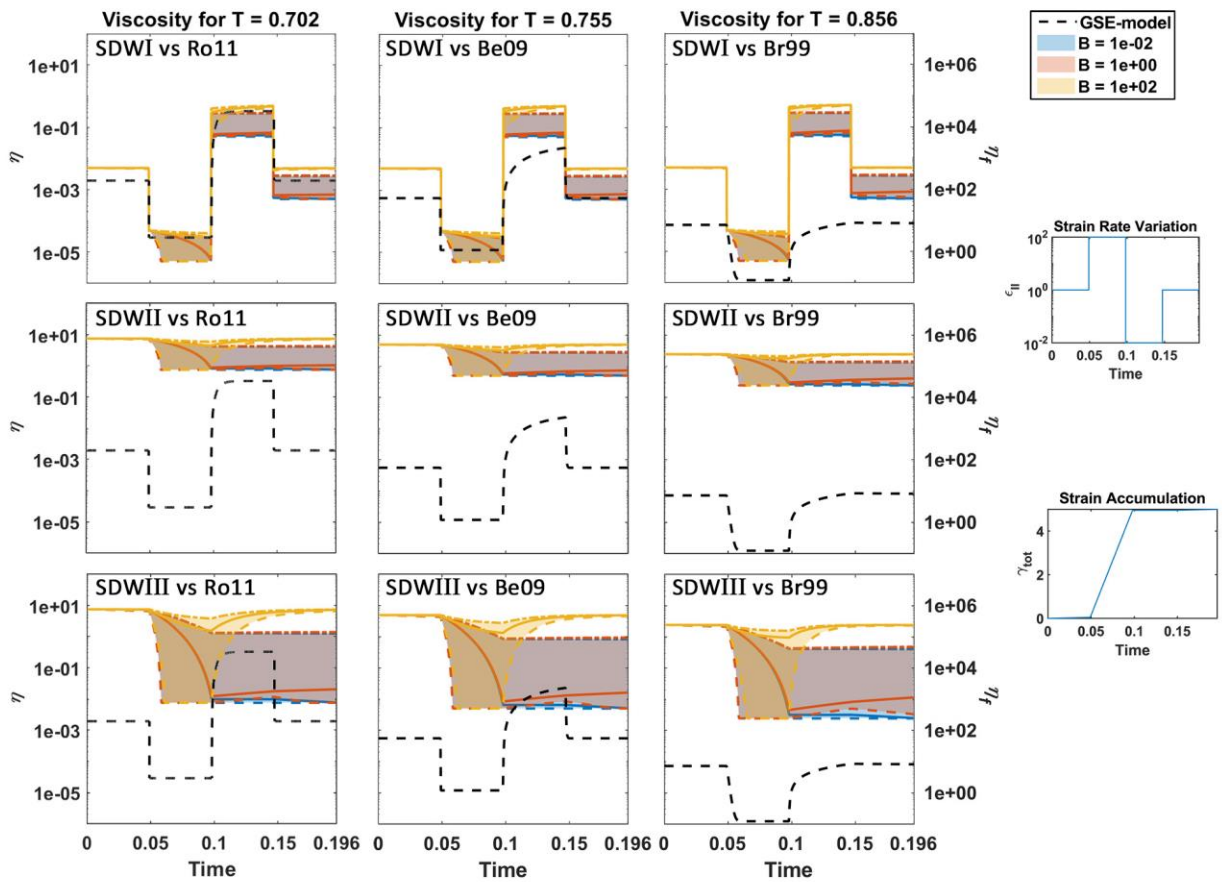

Figure 5. Variation of the diffusion creep viscosity η_f for a grain-size sensitive rheology (Br99, Be09, Ro11) and of the effective viscosity η for a visco-plastic rheology in combination with strain-dependent weakening for three different weakening methods (see eq. 7), for the intermediate temperature range, and a step like variation of the total strain rate $\dot{\varepsilon}_{II}$. The colored shaded area is the range of the weakened viscosity for different healing time scales B (blue: 10^{-2}: red: 1, yellow: 10^{2}) and critical strains γ_{cr} (dashed lines: 1, solid lines: 5, dash-dotted lines: 10). The smaller plots on the right show the variation of the total strain rate and the total strain γ_{tot} with time for each model. All parameters are scaled by the equations defined in supporting information S1.

During the first stage, strain is not high enough to observe any weakening for all SDW parameter combinations. When the total strain rate increases (at $t \approx 0.05$), strain-dependent weakening is observed leading to a maximum damage during the second stage (dashed lines) for all healing time scales B in combination with small critical strains, i.e. $\gamma_{cr} < 5$. If $\gamma_{cr} \geq 5$, only a modest decrease of the viscosity is observed for all healing time scales (solid lines), for which maximum damage is reached only at the end of the second stage if $B \leq 1$ and $\gamma_{cr} \sim 5$. Maximum damage is not reached if $B = 100$ and $\gamma_{cr} \geq 5$, only resulting in a slight decrease in viscosity due to SDW (clearly observable for Be09 and Br99). The overall weakening for a pseudo-plastic rheology including SDW is higher (~three orders of magnitude) than for GSE weakening (~two orders of magnitude). Assuming a smaller maximum damage $\mathcal{D}_{\max}$ (~ 60-80%) could result in a similar weakening effect due to SDW. The same applies to the increase of the total energy dissipation due weakening by deformational work for both rheologies (not shown here).

While weakening due to SDW in the second stage is too strong and slower in comparison to GSE, the hardening in the third stage shows a similar rate to grain growth if $B = 100$ and $\gamma_{cr} = 1$. In fact, at the end of the third stage, i.e. the healing stage, the default yield stress (or viscosity) is reached, similar to the approach toward a steady-state viscosity condition for the composite rheology. In the last stage, no further weakening or hardening is observable (as during the first stage). Damage does also not evolve further (or only slightly) during the last two stages for smaller healing time scales, i.e. for $B \leq 1$. Even for the highest temperature used in this temperature range ($T = 0.856$), only a minor healing effect is observed (Br99 in Figure 5).

In general, weakening happens almost instantly and is similar to the general yielding effect of a pseudo-plastic rheology. Including strain-dependent weakening enhances the weakening effect by ~one order of magnitude. The critical strain γ_{cr} controls the rate and effectiveness of the weakening, resulting in a faster (almost instant) weakening with a decreasing critical strain. The healing time scale B mainly governs the rate of damage reduction, resulting in a faster healing with an increasing healing time scale (it has only a minor effect on the weakening rate, if the critical strain is small). Assuming $B \leq 1$, hardening for a SDW rheology is significantly slower than hardening due to grain-size evolution. However, for a fast healing time scale ($B = 100$) and small critical strain ($\gamma_{cr} = 1$), the GSE behavior of the chosen GSE models is matched well by the hardening rate of SDW.

3.2.2 Viscous Strain Softening

Assuming that deformation only takes place in the viscous regime, we assume weakening is governed by viscous strain softening alone (SDW-II and SDW-III; in addition, we chose a large yield stress to avoid yielding); this significantly changes the transient behavior of the viscosity (middle and lower row in Figure 5). For SDW-II, maximum weakening is limited to ~one order of magnitude, which can be amplified to ~three orders of magnitude for SDW-III, by design. In the VSS regime, the damage effects are akin to the effects of plastic strain softening (SDW-I), without the additional yielding component. Similar to SDW-I, no significant damage is accumulated during the first stage. A sudden increase in the strain rate (at $t \approx 0.05$), leads to an immediate weakening effect, still slightly slower than due to GSE. The strongest time-dependency for SDW in the VSS regime is given by the fastest healing time scale ($B = 100$) and the smallest critical strain ($\gamma_{cr} = 1$; dashed, colored lines). Increasing the critical strain (i.e. $\gamma_{cr} > 1$) results in a less effective weakening during the second stage followed by no further damage during the last two stages. Even for smaller healing time scales (i.e. $B \leq 1$), no further variations in damage are observable (e.g. for $B = 0.01$ and $\gamma_{cr} = 10$, i.e. the dashed-dotted lines). For $B \leq 1$, weakening becomes significant only if $\gamma_{cr} < 5$ (solid and dashed lines). For such healing time scales ($B \leq 1$) and critical strains ($\gamma_{cr} < 5$) only a minor hardening is observable during the last two stages.

In general, maximum weakening is reached for small to intermediate critical strains, i.e. $\gamma_{cr} < 5$. In addition, the critical strain required to reach maximum damage decreases with a faster healing time scale B (i.e. maximum damage is reached for $B = 100$ only if $\gamma_{cr} = 1$). However, a clear hardening effect is only visible for $B = 100$, which shows a similar behavior to the damage evolution for plastic strain softening (SDW-I). Due to the missing yielding effect in viscous strain softening, the slight hardening during the last two stages for $B = 1$ and $\gamma_{cr} < 5$ becomes more prominent in comparison to SDW-I. With respect to the GSE behavior, the hardening rate is slightly slower than grain growth, especially for Ro11. Overall, strength variations due to viscous strain softening clearly differ from the strength evolution for GSE. However, using a viscous strain softening mechanism emphasizes the effect of strain memory due to SDW, considering the continuously lower effective viscosities for $B \leq 1$.

Still assuming that deformation takes place in the viscous regime, but with larger weakening (SDW-III), shows a similar trend as for SDW-II. Maximum weakening is also only reached for $\gamma_{cr} = 1$ and hardening is most effective for the largest healing time scale ($B = 100$). Still, hardening for such a viscous strain softening mechanism remains slightly slower in comparison to GSE but, in addition, weakening in the second stage becomes too strong (~ 3 orders of magnitude with respect to ~ 2). The stronger weakening, however, further emphasizes the variations for $B \leq 1$ and $\gamma_{cr} < 5$ during the last two stages. Therefore, the SDW-III mechanism highlights a stronger time-dependency in SDW for a decreasing critical strain, even for higher healing time scales (i.e. $B \geq 1$).

Overall, the weakening captured by viscous strain softening resembles GSE, providing an instant reduction in viscosity, although with slightly slower weakening rates. Hardening within a viscous strain softening rheology, however, fails to resemble the full transient behavior of GSE. Since the initial state is defined by the temperature alone and cannot be exceeded by the hardening during a later stage, the maximum viscosity is limited by the initial condition. Thus, starting in an undeformed state does not result in further hardening due to strain reduction once all deformation is removed resulting in a significantly different transient behavior than due to grain-size evolution. Viscous strain softening, however, emphasizes transient effects which also govern the behavior for plastic strain softening.

Similar transient behaviors in the viscosities for both rheologies, VSS and PSS, are observable at even lower temperatures (cf. supporting information Figure S2). Hardening is significantly slowed so that at the end of the last stage, some damage remains, even for $\gamma_{cr} = 1$. This shows the strong effect of temperature on the healing rate in the SDW rheology.

3.2.3 Strain-Rate Variation Versus Total Strain

Varying the strain rate over a certain amount of accumulated strain (Figure 6) highlights different aspects of the temporal behavior for SDW and GSE. For the SDW rheology, prolonged deformation leads to higher damage, resulting in a clear weakening during the first and last stage of the experiment, for $B \leq 1$. This was not observed in the constant time test. The more effective weakening is most significant for $\gamma_{cr} = 1$. During the healing step, more effective hardening is seen for $B \geq 1$. Most of the hardening takes place in the beginning of the healing stage, completely removing the damage. Consequently, no strength reduction is observed at the end of the healing stage. If $B = 0.01$, however, the strain remains preserved. A shorter time during the intermediate to high strain rate stages ($\dot{\varepsilon}_{II} \geq 1$; or dimensional 10^{-14} s^{-1}) decreases damage accumulation and reduces weakening in the second stage. The different weakening mechanisms (SDW-I – SDW-III) show the same temporal behavior, whereas their major differences are emphasized by the lag of yielding and the additional power exponent, respectively, as before.

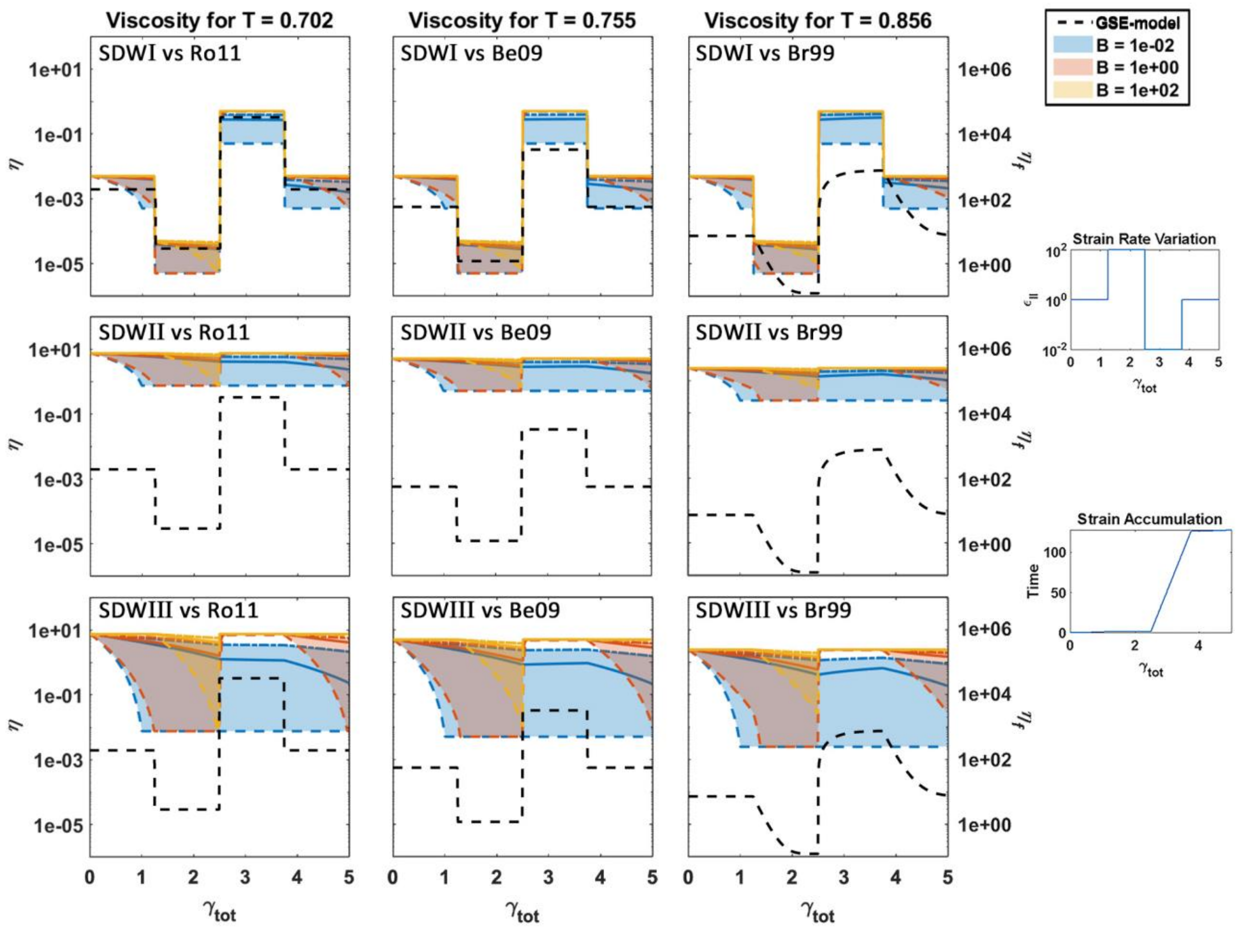

Figure 6. Variation of the diffusion creep viscosity η_f for a grain size sensitive rheology (Br99, Be09, Ro11) and of the effective viscosity η for a visco-plastic rheology in combination with strain dependent weakening for three different weakening methods (see eq. 7) over the total strain γ_{tot}, for the intermediate temperature range, and a step like change of the total strain rate $\dot{\varepsilon}_{II}$. The colored shaded area is the range of the weakened viscosity for different healing time scales B (blue: 10^{-2}, red: 1, yellow: 10^{2}) and critical strains γ_{cr} (dashed lines: 1, solid lines: 5, dash-dotted lines: 10). The smaller plots on the side show the variation of the strain rate and the time for the total strain γ_{tot} for each model. All parameters are scaled by the equations defined in supporting information S1.

Since grain size reduction is almost instant (except for Br99), weakening due to dynamic recrystallization is not affected by changing the reference parameter to the total strain γ_{tot} and, as before, this yields in an instant weakening by a factor of ~two orders of magnitude. The prolonged time in the hardening stage, however, shows different behavior, resulting in an instant hardening due to grain growth and a viscosity increase of ~three to four orders of magnitude. The different time periods during each segment result in an even less time-sensitive behavior for GSE in comparison to the previous experiment; their behavior is reminiscent of the viscosity variations due to plastic yielding (except for Br99).

Using strain control thus emphasizes the difference of the memory effects of SDW and GSE. The reduced weakening stage emphasizes the time lag between weakening due to SDW and grain-size reduction. The prolonged time, on the other hand, accentuates the similarity between the healing rate for SDW and grain growth. In general, these experiments emphasize the strong strain memory effect for SDW, instant hardening during the healing stage comparable to grain growth, and a slower, but more effective, weakening in comparison to grain size reduction.

4 Discussion

4.1 Damage Memory in a Lithospheric Shear Zone

With this general behavior as background, we seek to further explore the effects of damage evolution for lithospheric weak zones as an analog for an evolving plate boundary. We assume an initially undeformed state and compare a pseudo-plastic rheology without (dotted lines in Figure 7) and with SDW (colored lines with shading). We assume that the shear zone is at the transition to yielding, i.e. the viscous stress is equal to the yield stress and the yield viscosity is equal to the temperature dependent viscosity. The effective viscosity of the pseudo-plastic rheology and SDW is only governed by plastic strain softening (i.e. SDW-I), and the strain rate varies in the same way as previously discussed.

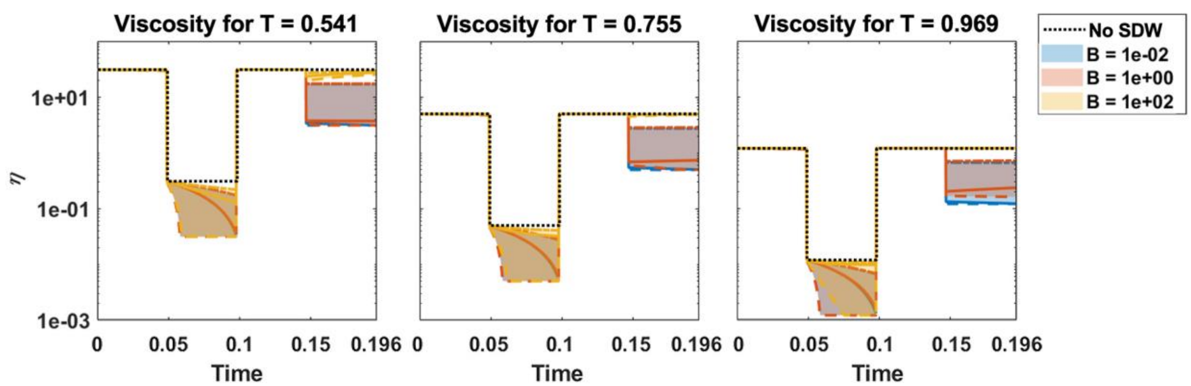

Figure 7. Strain-dependent weakening and strain memory effect for a theoretical plastic fault zone for three different non-dimensional temperatures. The strain rate varies step-like in the same manner as in the previous examples, whereas the yield stress is defined by the initial strain rate and the temperature dependent viscosity, i.e. the material is at the yield transition in the beginning.

This setup prohibits a viscosity increase in the third stage due to the limitation by the temperature dependent viscosity and highlights the effects of damage memory during the last stage. The accumulated strain during the second stage results in a decrease of the yield stress. Damage is fully preserved for $B \leq 1$ for all temperatures, while only a fraction of the damage is preserved for $B = 100$ at the lowest temperature. This damage memory enables weakening during the last stage due to the reduced yield stress, which is, of course, not a feature of pure visco-plastic rheology. This behavior is similar to what was discussed above, but Figure 7 emphasizes the importance of temperature on transient behavior of shear zones which is controlled by the healing time scale B and the activation energy of the healing rate η_2.

We can now return to the question of the duration over which such a synthetic suture remains weakened for the different rheological descriptions. The healing time scales and activation energies employed so far lie within the range of the growth rates inferred from laboratory grain-size evolution laws (Figure 1). However, to more widely, and perhaps more realistically, explore the parameters, we analyzed the healing time of a lithospheric shear zone assuming a vertical deformation zone and an oceanic geotherm (Figure 8). For the geotherm we assume a half-space cooling model for an oceanic lithosphere of 120 Ma age with constant thermal parameters and a potential mantle temperature of 1315 °C. As an initial condition, we assume a steady-state grain size at a background strain rate of 10^{-15} s^{-1} within the shear zone that might mimic a nearly rigid plate. We then calculate the grain-size reduction along a one-dimensional temperature profile for a sudden strain rate increase (up to 7 orders of magnitude), say due to enhanced tectonic deformation (side stepping the issue of nucleation). A similar analysis is feasible assuming constant stress conditions, but due to kinematic nature of our previous experiments we focus on the constant strain-rate approach. Based on the weakening behavior discussed above, we assume that the steady-state grain size responds instantly. Assuming the strain-rate is reduced to its initial value after this deformation episode, we calculated the time (t_h) for the effective viscosity and for the grain size to reach steady-state again (within 1 and 0.1%, respectively) solving eq. (10) using a dry, composite rheology (Hirth & Kohlstedt, 2003) and GSE of Ro11 and Be09 (Figures 8a and b). Additionally, we show the time to reduce the accumulated damage by 95% (cf. supporting information eq. S9) for $B = 10^{-12}$ – 10^{-16} s^{-1} (i.e. with decreasing B, the healing time increases).

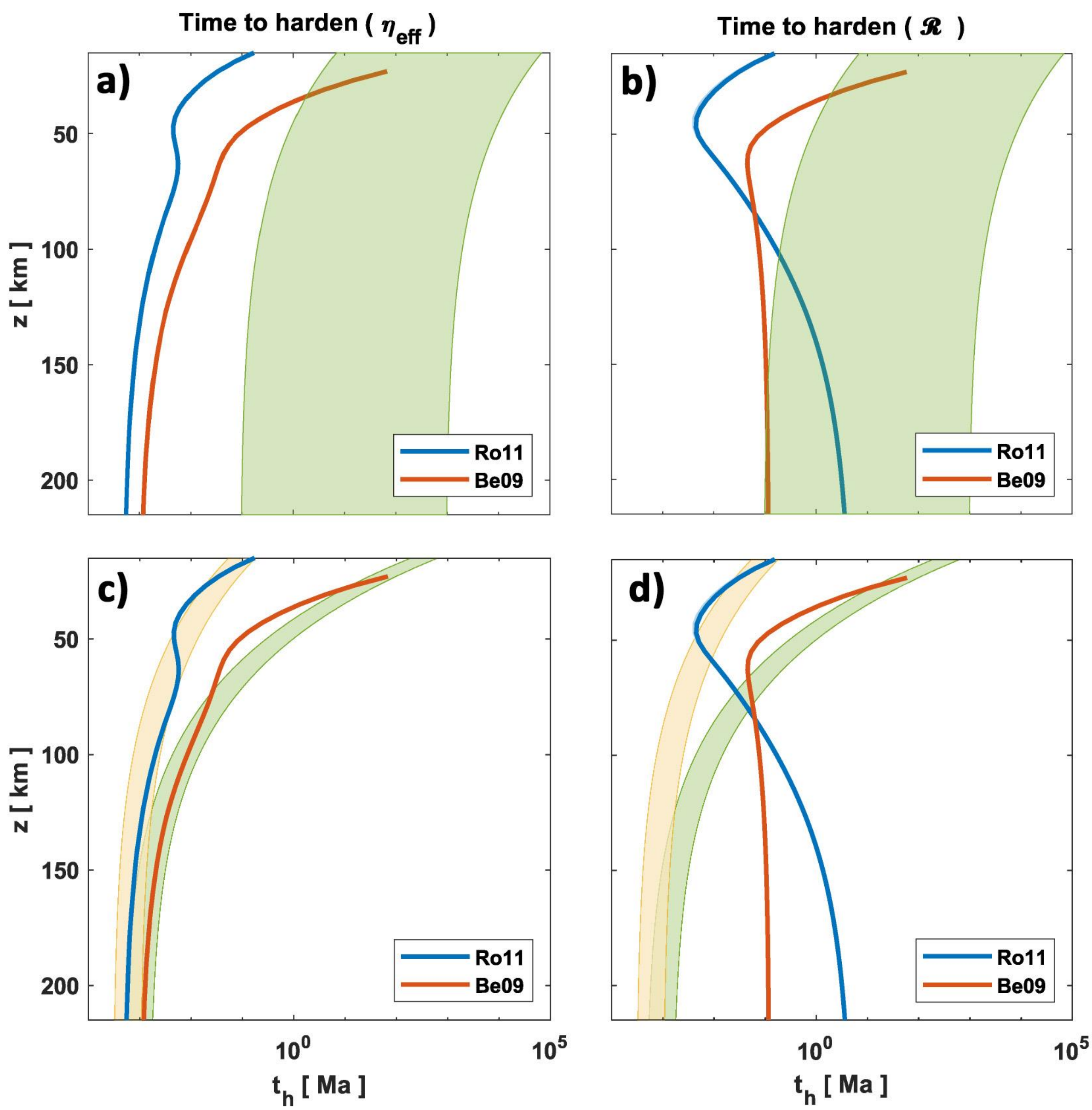

Figure 8. Hardening time in a vertical shear zone assuming an oceanic geotherm and constant strain rate using a SDW rheology or a composite rheology in combination with GSE. a) Time t_h in [Ma] to reach η_{eff} at a constant strain rate ($\dot{\varepsilon}_{II} = 10^{-15}$ s^{-1}) and range of hardening for SDW assuming $B = 10^{-16} - 10^{-12}$ s^{-1} (shaded area). b) Time t_h in [Ma] to reach the steady-state grain size for Ro11 and Be09 (solid lines) and SDW hardening time same as in (a). c and d) Same GSE hardening time as in (a) and (b), but range of SDW hardening time fitted to η_{eff} curve of Ro11 (yellow shaded area; $B = 9{\cdot}10^{-11} - 3{\cdot}10^{-10}$ s^{-1} and $\eta_2 = 27.631$) and Be09 (green shaded area; $B = 6{\cdot}10^{-11} - 2{\cdot}10^{-10}$ s^{-1} and $\eta_2 = 69.078$).

The results show, that the healing time t_h does not depend on the actual grain size and is thus independent of the amount of deformation; it is, however, strongly governed by temperature. The same is true for the reduction of strain as defined in supporting information eq. (S9). Within the shear zone, the healing times for grain growth are well matched by the strain reduction rates of the simplified description (Figures 8a and b), assuming a large B (similar to what was discussed above), especially in the lower part of the profile (for both GSE models) and partly within the upper part (for Be09). However, for most of the ranges of B so far considered the healing time for SDW is too slow in comparison to Ro11 and Be09. In addition, with respect to the effective viscosity, the slope of the healing time curve (governed by η_2) is not matched as well.

Varying η_2 and B, we can fit the healing time t_h for strain-dependent weakening to the healing time for the effective viscosity of grain-size evolution. For Ro11, a range of $B = 9 \cdot 10^{-11}$ - $3 \cdot 10^{-10}$ s^{-1} and $\eta_2 = 27.631$ and for Be09 a range of $B = 6 \cdot 10^{-11}$ - $2 \cdot 10^{-10}$ s^{-1} and $\eta_2 = 69.078$ lead to the best match, assuming damage is almost completely removed and the strength of the shear zone is defined by the effective viscosity. While the fitted healing time also matches the rates for the grain-size evolution within the upper part of the lithosphere, it is too fast within the lower part of the shear zone. However, the grain size only controls the effective viscosity within the upper part of the lithosphere anyway, and dislocation creep dominates in the deeper regions (below ~ 60 and 70 km depth for Ro11 and Be09, respectively). Thus, the healing time for strain-dependent weakening can approximate the healing behavior for grain growth in a composite rheology.

This comparison shows that grain-size sensitive viscous rheologies, as explored widely for memory dependent convection, could potentially be substituted efficiently in long-term mantle convection models by a simplified strain weakening/hardening rheology under the parameter choices discussed above. As noted above, the rheological weakening and hardening described by GSE is only one potential microphysical weakening mechanism, however. A SDW parameterization may indeed also capture other mechanisms, such as mineral transformations or serpentinization/mylonitization (e.g. Bos and Spiers, 2002; Huismans and Beaumont, 2007), fluid/melt percolation, or hydration along forming brittle fractures (e.g. Gerya, 2013). The opposite, however, is not necessarily true as grain-size evolution itself may not be efficient enough to resemble the full spectrum of lithospheric localization behavior (e.g. Montesi & Hirth, 2003; Montesi, 2003), for example for the case of transform faults (Schierjott et al., 2020).

4.2 Plastic Strain Softening Versus Grain-Size Reduction Weakening

The overall weakening effect for a plastic strain softening and composite, grain-size sensitive rheology can be compared considering an effective strain-rate exponent. Assuming the system is in steady-state and computing the grain size based on strain rate (supporting information eqs. S25-S26), the diffusion creep viscosity, and thus weakening due to grain size reduction, is given by the dislocation creep strain rate with an effective strain-rate exponent

$$\eta_f \sim \dot{\varepsilon}_{II,l}^{-\frac{m(1+n)}{n(p+1)}} . \tag{14}$$

With the rheological parameters from Hirth and Kohlstedt (2003), $m = 3$, and the parameter range for p from the different GSE models (p = *2…4*, see supporting information S1) the effective strain-rate exponent of viscosity dependence is between ~ –0.8 and –1.3, compared to $-(n-1)/n \sim -0.7$ for pure dislocation creep at $n = 3.5$. When expressed in terms of stress instead of strain rate, the viscosity scales with stress to the power of $-m(n+1)/(p+1) \sim -4.5$ …

-2.7 compared to $1 - n = -2.5$ for dislocation creep. The effective strain-rate exponent for a pseudo-plastic rheology is unity (eq. 2) and falls into the range of an effective exponent for diffusion creep deformation with steady-state grain size.

Considering instant weakening in GSE due to grain-size reduction, the steady-state approximation is suitable to describe weakening. The weakening described by eq. (14), however, only addresses the diffusion creep contribution due to a variation of the dislocation creep strain rate. Considering that the dislocation creep strain rate decreases for a more dominant diffusion creep deformation, weakening due to grain size reduction becomes less effective. Therefore, it is only close to the transition between dislocation and diffusion creep where weakening due to grain-size reduction can be approximated by plastic yielding. That said, a change in viscosity due to grain-size reduction is almost of the same order of magnitude as a change in viscosity due to plastic yielding. The choice of a small critical strain (e.g. $\gamma_{cr} = 1$) and a moderate damage parameter ($\mathcal{D}_{max}$ ~ 60-80 %) for a plastic strain softening rheology serves to best approximate the weakening behavior expected from grain size reduction.

5 Conclusions

Our study explores similarities and differences between the memory-dependent weakening expected from the various grain-size evolution and strain-dependent weakening formulations that are currently in use in lithospheric and mantle dynamic modeling. The weakening effect of pure pseudo-plastic failure is similar to the near-instant weakening for grain-size evolution and adding strain-dependence further enhances weakening. The combination of a small critical strain ($\gamma_{cr} = 1$) and moderate maximum damage ($\mathcal{D}_{max}$ ~ 60-80%) in the plastic strain softening (PSS) rheology has a similar effect as grain-size reduction. Weakening due to a viscous strain softening (VSS) rheology, however, is not instantaneous and, thus, cannot match the rate of weakening of grain size reduction. To match the amount of weakening by grain-size reduction, VSS also requires an amplified maximum weakening.

A pure pseudo-plastic rheology does, by definition, also not possess a hardening component, and has a much faster healing time scale as the strain-rate decreases. Assuming strain-dependent weakening can model a healing behavior that is similar to the hardening due to grain growth as described by a wattmeter. However, the healing behavior for a VSS rheology fails to approximate grain growth strengthening. The rate, governed by B and η_2, can be similar to the grain growth rate, but VSS does not enable hardening larger than the ‘undamaged’ state. This is, however, crucial for the composite dislocation-diffusion creep rheology expected for the uppermost mantle, which is governed by grain size and temperature, respectively. On the other hand, plastic strain softening and the associated yielding implementation do not only resemble the amount of healing due to grain growth, but also its rate.

In particular, for the grain-size evolution models explored, the healing time scale B ~ $6{\cdot}10^{-11}$ - $3{\cdot}10^{-10}$ s^{-1} and an activation energy of η_2 ~ 30 – 70 best approximate the time scales for grain growth in a composite rheology. Therefore, the plastic strain softening rheology does indeed enable a “realistic” hysteresis effect with a memory duration that is similar to that expected for grain growth for lithospheric temperature conditions. This allows modeling the formation, maintenance, and reactivation of lithospheric weak zones, but precludes further weakening in the deeper mantle due to the higher temperatures and faster healing. Our results help to identify the features and parameter ranges needed to represent grain-size evolution laws and their associated rheologies with simplified approaches. Additional comparisons with laboratory and field observations using this simplified framework may serve to resolve outstanding questions of plate tectonic strain localization.

Acknowledgments

We acknowledge discussions with Nicolas Coltice and the Valflaunès Chateau group. TWB was partially supported by NSF EAR 1927216 and 1853856. We would also like to thank Taras V. Gerya and an anonymous reviewer for their constructive comments that helped to improve the manuscript. Datasets for this research are included in these papers: Braun et al. (1999), Behn et al. (2009), Rozel et al. (2011), and Dannberg et al. (2017). No new data were created for this research.

References

Atkinson, H. V. (1988). Overview no. 65: Theories of normal grain growth in pure single phase systems. *Acta Metallurgica*, 36(3), pp. 469-491. https://doi.org/10.1016/0001-6160(88)90079-X.

Audet, P., & Bürgmann, R. (2011). Dominant role of tectonic inheritance in supercontinent cycles. *Nature Geoscience*, 4(3), pp. 184-187. https://doi.org/10.1016/0001-6160(88)90079-X.

Austin, N. & Evans, B. (2007). Paleowattmeters: A scaling relation for dynamically recrystallized grain size. *Geology*, 35(4), pp. 343-346. https://doi.org/10.1130/G23244A.1

Barr, A. C., & McKinnon, W. B. (2007). Convection in ice I shells and mantles with self-consistent grain size. *Journal of Geophysical Research: Planets*, 112(E2). https://doi.org/10.1029/2006JE002781.

Becker, T. W., Kustowski, B., & Ekström, G. (2008). Radial seismic anisotropy as a constraint for upper mantle rheology. *Earth and Planetary Science Letters*, 267(1-2), 213-227. https://doi.org/10.1016/j.epsl.2007.11.038.

Behn, M. D., Hirth, G. & Elsenbeck II, J. R. (2009). Implications of grain size evolution on the seismic structure of the oceanic upper mantle. *Earth and Planetary Science Letters*, 282(1-4), pp. 178-189. https://doi.org/10.1016/j.epsl.2009.03.014.

Bercovici, D. (1993). A simple model of plate generation from mantle flow. *Geophysical Journal International*, 114(3), pp. 635-650. https://doi.org/10.1111/j.1365-246X.1993.tb06993.x.

Bercovici, D. (1995). A source-sink model of the generation of plate tectonics from non-Newtonian mantle flow. *Journal of Geophysical Research: Solid Earth*, 100(B2), pp. 2013-2030. https://doi.org/10.1029/94JB02598.

Bercovici, D. (2003). The generation of plate tectonics from mantle convection. *Earth and Planetary Science Letters*, 205(3-4), pp. 107-121. https://doi.org/10.1016/S0012-821X(02)01009-9.

Bercovici, D., & Ricard, Y. (2005). Tectonic plate generation and two-phase damage: Void growth versus grain size reduction. *Journal of Geophysical Research: Solid Earth*, 110(B3). https://doi.org/10.1029/2004JB003181.

Bercovici, D. & Ricard, Y. (2012). Mechanisms for the generation of plate tectonics by two-phase grain-damage and pinning. *Physics of the Earth and Planetary Interiors,* Volume 202, pp. 27-55. https://doi.org/10.1016/j.pepi.2012.05.003.

Bercovici, D. & Ricard, Y. (2013). Generation of plate tectonics with two-phase grain-damage and pinning: Source-sink model and toroidal flow. *Earth and Planetary Science Letters,* Volume 365, pp. 275-288. https://doi.org/10.1016/j.epsl.2013.02.002.

Bercovici, D. & Ricard, Y. (2014). Plate tectonics, damage and inheritance. *Nature*, 508(7497), p. 513. https://doi.org/10.1038/nature13072.

Bercovici, D., & Ricard, Y. (2016). Grain-damage hysteresis and plate tectonic states. *Physics of the Earth and Planetary Interiors*, 253, 31-47. https://doi.org/10.1016/j.pepi.2016.01.005.

Bercovici, D., Tackley, P., & Ricard, Y. (2015). 7.07-the generation of plate tectonics from mantle dynamics. *Treatise on Geophysics*. Elsevier, Oxford, 271-318. https://doi.org/10.1016/B978-0-444-53802-4.00135-4.

Bos, B., & Spiers, C. J. (2002). Frictional-viscous flow of phyllosilicate-bearing fault rock: Microphysical model and implications for crustal strength profiles. *Journal of Geophysical Research: Solid Earth*, 107(B2), ECV-1. https://doi.org/10.1029/2001JB000301

Braun, J. et al. (1999). A simple parameterization of strain localization in the ductile regime due to grain size reduction: A case study for olivine. *Journal of Geophysical Research: Solid Earth,* 104(B11), pp. 25167-25181. https://doi.org/10.1029/1999JB900214.

Brune, S., Heine, C., Pérez-Gussinyé, M. & Sobolev, S. V. (2014). Rift migration explains continental margin asymmetry and crustal hyper-extension. *Nature Communications,* 5 (1), pp. 1-9. https://doi.org/10.1038/ncomms5014.

Burov, E. B. (2011). Rheology and strength of the lithosphere. *Marine and Petroleum Geology*, Volume 28(8), pp. 1402-1443. https://doi.org/10.1016/j.marpetgeo.2011.05.008.

Crameri, F., Tackley, P. J., Meilick, I., Gerya, T. V., and Kaus, B. J. P. (2012), A free plate surface and weak oceanic crust produce single-sided subduction on Earth, *Geophys. Res. Lett.*, 39, L03306, doi:10.1029/2011GL050046.

Coltice, N., Gérault, M. & Ulvrová, M. (2017). A mantle convection perspective on global tectonics. *Earth Science Reviews,* Volume 165, pp. 120-150. https://doi.org/10.1016/j.earscirev.2016.11.006.

Coltice, N., Husson, L., Faccenna, C. & Arnould, M. (2010). What drives tectonic plates?. *Science advances*, 5(10), p. eaax4295. https://doi.org/10.1126/sciadv.aax4295.

Coltice, N., Rolf, T., Tackley, P. J., & Labrosse, S. (2012). Dynamic causes of the relation between area and age of the ocean floor. Science, 336(6079), 335-338. doi: 10.1126/science.1219120.

Dannberg, J., Eilon, Z., Faul, U., Gassmöller, R., Moulik, P., & Myhill, R. (2017). The importance of grain size to mantle dynamics and seismological observations. *Geochemistry, Geophysics, Geosystems*, 18(8), 3034-3061. https://doi.org/10.1002/2017GC006944.

de Bresser, J., Peach, C., Reijs, J. & Spiers, C. (1998). On dynamic recrystallization during solid state flow: Effects of stress and temperature. *Geophysical Research Letters,* 25(18), pp. 3457-3460. https://doi.org/10.1029/98GL02690.

Enns, A., Becker, T. & Schmeling, H. (2005). The dynamics of subduction and trench migration for viscosity stratification. *Geophysical Journal International,* 160(2), pp. 761-775. https://doi.org/10.1111/j.1365-246X.2005.02519.x.

Evans, B., Renner, J. & Hirth, G. (2001). A few remarks on the kinetics of static grain growth in rocks. *International Journal of Earth Sciences,* 90(1), pp. 88-103. https://doi.org/10.1007/s005310000150.

Faul, U. H. & Scott, D. (2006). Grain growth in partially molten olivine aggregates. *Contributions to Mineralogy and Petrology,* 151(1), pp. 101-111. https://doi.org/10.1007/s00410-005-0048-1.

Faul, U. H., & Jackson, I. (2007). Diffusion creep of dry, melt-free olivine. *Journal of Geophysical Research: Solid Earth*, 112(B4). https://doi.org/10.1029/2006JB004586.

Foley, B. J. (2018). On the dynamics of coupled grain size evolution and shear heating in lithospheric shear zones. *Physics of the Earth and Planetary Interiors*, 283, 7-25. https://doi.org/10.1016/j.pepi.2018.07.008.

Foley, B. & Becker, T. (2009). Generation of plate-like behavior and mantle heterogeneity from a spherical, viscoplastic convection model. *Geochemistry, Geophysics, Geosystems,* Volume 612, pp. 18-25. https://doi.org/10.1029/2009GC002378.

Foley, B. J., & Rizo, H. (2017). Long-term preservation of early formed mantle heterogeneity by mobile lid convection: importance of grainsize evolution. *Earth and Planetary Science Letters*, 475, 94-105. https://doi.org/10.1016/j.epsl.2017.07.031.

Fuchs, L. & Becker, T. W. (2019). Role of strain-dependent weakening memory on the style of mantle convection and plate boundary stability. *Geophysical Journal International,* 218(1), pp. 601-618. https://doi.org/10.1093/gji/ggz167.

Gerya, T. V. (2013). Three-dimensional thermomechanical modeling of oceanic spreading initiation and evolution. *Physics of the Earth and Planetary Interiors*, 214, 35-52. https://doi.org/10.1016/j.pepi.2012.10.007.

Hansen, L. N., Zimmerman, M. E., Dillman, A. M., & Kohlstedt, D. L. (2012). Strain localization in olivine aggregates at high temperature: A laboratory comparison of constant-strain-rate and constant-stress boundary conditions. *Earth and Planetary Science Letters,* 333, pp. 134-145. https://doi.org/10.1016/j.epsl.2012.04.016.

Hieronymus, C. F. (2006). Time-dependent strain localization in viscous media with state-dependent viscosity. *Physics of The Earth and Planetary Interiors*, 157(3-4), pp. 151-163. https://doi.org/10.1016/j.pepi.2006.03.020.

Hillert, M. (1965). On the theory of normal and abnormal grain growth. *Acta Metallurgica,* 13(3), pp. 227-238. https://doi.org/10.1016/0001-6160(65)90200-2.

Hiraga, T., Tachibana, C., Ohashi, N. & Sano, S. (2010). Grain growth systematics for forsterite±enstatite aggregates: Effect of lithology on grain size in the upper mantle. *Earth and Planetary Science Letters*, 291((1-4)), pp. 10-20. https://doi.org/10.1016/j.epsl.2009.12.026.

Hirth, G. & Kohlstedt, D. (1995). Experimental constraints on the dynamics of the partially molten upper mantle: Deformation in the diffusion creep regime. *Journal of Geophysical Research: Solid Earth*, 100(B2), pp. 1981-2001. https://doi.org/10.1029/94JB02128.

Hirth, G., & Kohlstedt, D. (2003). Rheology of the upper mantle and the mantle wedge: A view from the experimentalists. *GEOPHYSICAL MONOGRAPH-AMERICAN GEOPHYSICAL UNION*, 138, 83-106.

Höink, T., Lenardic, A., & Richards, M. (2012). Depth-dependent viscosity and mantle stress amplification: implications for the role of the asthenosphere in maintaining plate tectonics. *Geophysical Journal International*, 191(1), 30-41. https://doi.org/10.1111/j.1365-246X.2012.05621.x.

Huismans, R. & Beaumont, C. (2003). Symmetric and asymmetric lithospheric extension: Relative effects of fritconal-plastic and viscou strain softening. *Journal of Geophysical Research: Solid Earth*, 108(B10). https://doi.org/10.1029/2002JB002026.

Huismans, R. & Beaumont, C. (2007). Roles of lithospheric strain softening and heterogeneity in determining the geometry of rifts and continental margins. *Geological Society, London, Special Publications*, 282(1), pp. 11-138. https://doi.org/10.1144/SP282.6.

Jacoby, W. R., & Schmeling, H. (1981). Convection experiments and the driving mechanism. *Geologische Rundschau*, 70(1), pp. 207-230. https://doi.org/10.1007/BF01764323.

Kameyama, M., Yuen, D. A., & Fujimoto, H. (1997). The interaction of viscous heating with grain-size dependent rheology in the formation of localized slip zones. *Geophysical Research Letters*, 24(20), pp. 2523-2526. https://doi.org/10.1029/97GL02648.

Karato, S. (1989). Grain growth kinetics in olivine aggregates. *Tectonophysics*, 168(4), pp. 255-273. https://doi.org/10.1016/0040-1951(89)90221-7.

Karato, S. I., Toriumi, M., & Fujii, T. (1980). Dynamic recrystallization of olivine single crystals during high-temperature creep. *Geophysical Research Letters*, 7(9), 649-652. https://doi.org/10.1029/GL007i009p00649.

King, S. D., Gable, C. W. & Weinstein, S. A. (1992). Models of convection-driven tectonic plates: a comparison of methods and results. *Geophysical Journal International*, 109(3), pp. 481-487. https://doi.org/10.1111/j.1365-246X.1992.tb00111.x.

Kiss, D., Candioti, L. G., Duretz, T., & Schmalholz, S. M. (2020). Thermal softening induced subduction initiation at a passive margin. *Geophysical Journal International*, 220(3), pp. 2068-2073. https://doi.org/10.1093/gji/ggz572.

Kohlstedt, D., Evans, B. & Mackwell, S. (1995). Strength of the lithosphere: Constraints imposed by laboratory experiments. *Jounral of Geophysical Research: Solid Earth*, 100(B9), pp. 17587-17602. https://doi.org/10.1029/95JB01460.

Landuyt, W., & Bercovici, D. (2009). Variations in planetary convection via the effect of climate on damage. *Earth and Planetary Science Letters*, 277(1-2), 29-37. https://doi.org/10.1016/j.epsl.2008.09.034.

Lavier, L., Buck, W. & Polilakov, A. N. B. (2000). Factors controlling normal fault offset in an ideal brittle layer. *Journal of Geopysical Research: Solid Earth,* 105(B10), pp. 23431-23442. https://doi.org/10.1029/2000JB900108.

Mazzotti, S., & Gueydan, F. (2018). Control of tectonic inheritance on continental intraplate strain rate and seismicity. *Tectonophysics*, 746, pp. 602-610. https://doi.org/10.1016/j.tecto.2017.12.014.

Mei, S. & Kohlstedt, D. L. (2000). Influence of water on plastic deformation of olivine aggregates: 1. Diffusion creep regime. *Journal of Geophysical Research: Solid Earth*, 105(B9), pp. 21457-21469. https://doi.org/10.1029/2000JB900179.

Montési, L. (2013). Fabric development as the jey for forming ductile shear zones and enabling plate tectonics. *Journal of Structural Geology,* Volume 50, pp. 254-266. https://doi.org/10.1016/j.jsg.2012.12.011.

Montési, L. & Hirth, G. (2003). Grain size evolution and the rheology of ductile shear zones: from laboratory experiments to postseismic creep. *Earth and Planetary Sciences Letters,* 211(1-2), pp. 97-110. https://doi.org/10.1016/S0012-821X(03)00196-1.

Moresi, L., & Solomatov, V. (1998). Mantle convection with a brittle lithosphere: thoughts on the global tectonic styles of the Earth and Venus. *Geophysical Journal International*, 133(3), 669-682. https://doi.org/10.1046/j.1365-246X.1998.00521.x.

Mulyukova, E., & Bercovici, D. (2017). Formation of lithospheric shear zones: effect of temperature on two-phase grain damage. *Physics of the Earth and Planetary Interiors*, 270, 195-212. https://doi.org/10.1016/j.pepi.2017.07.011.

Mulyukova, E., & Bercovici, D. (2018). Collapse of passive margins by lithospheric damage and plunging grain size. *Earth and Planetary Science Letters*, 484, 341-352. https://doi.org/10.1016/j.epsl.2017.12.022.

Nichols, S. J. & Mackwell, S. J. (1991). Grain growth in porous olivine aggregates. *Physics and Chemistry of Minerals*, 18(4), pp. 269-278. https://doi.org/10.1007/BF00202580.

Ogawa, M. (2003). Plate-like regime of a numerically modeled thermal convection in a fluid with temperature-, pressure-, and stress-history-dependent viscosity. *Journal of Geophysical Research: Solid Earth,* 108(B2). https://doi.org/10.1029/2000JB000069.

Platt, J. P., & Behr, W. M. (2011). Grainsize evolution in ductile shear zones: Implications for strain localization and the strength of the lithosphere. *Journal of Structural Geology*, 33(4), pp. 537-550. https://doi.org/10.1016/j.jsg.2011.01.018.

Précigout, J., & Almqvist, B. S. (2014). The Ronda peridotite (Spain): A natural template for seismic anisotropy in subduction wedges. *Geophysical Research Letters*, 41(24), pp. 8752-8758. https://doi.org/10.1002/2014GL062547.

Ricard, Y. & Bercovici, D. (2009). A continuum theory of grain size evolution and damage. *Journal of Geophysical Research: Solid Earth*, 114(B1). https://doi.org/10.1029/2007JB005491

Rozel, A., Ricard, Y. & Bercovici, D. (2011). A thermodynamically self-consistent damage equation for grain size evolution during dynamic recrystallization. *Geophysical Journal International*, 184(2), pp. 719-728. https://doi.org/10.1111/j.1365-246X.2010.04875.x.

Ruh, J., Gerya, T. & Burg, J. (2014). 3D effects of strain vs. velocity weakening on deformation patterns in accretionary wedges. *Tectonophysics,* Volume 615, pp. 122-141. https://doi.org/10.1016/j.tecto.2014.01.003.

Solomatov, V. S. (2001). Grain size-dependent viscosity convection and the thermal evolution of the Earth. *Earth and Planetary Science Letters*, 191(3-4), pp. 203-212. https://doi.org/10.1016/S0012-821X(01)00426-5.

Speciale, P. A., Behr, W. M., Hirth, G., & Tokle, L. (2020). Rates of olivine grain growth during dynamic recrystallization and post-deformation annealing. Journal of Geophysical Research: Solid Earth, 125, e2020JB020415. https://doi.org/10.1029/2020JB020415

Schierjott, J. C., Thielmann, M., Rozel, A. B., Golabek, G. J., & Gerya, T. V. (2020). Can grain size reduction initiate transform faults?—Insights from a 3-D numerical study. Tectonics, 39, e2019TC005793. https://doi.org/10.1029/2019TC005793

Schubert, G., & Turcotte, D. L. (1972). One-dimensional model of shallow-mantle convection. *Journal of Geophysical Research*, 77(5), pp. 945-951. https://doi.org/10.1029/JB077i005p00945.

Tackley, P. J. (2000a). The quest for self-consistent generation of plate tectonics in mantle convection models. *Geophysical Monograph-American Geophysical Union*, 121, 47-72.

Tackley, P. J. (2000b). Self-consistent generation of tectonics plates in timedependent, three-dimensional mantle convection simulations: 1. Pseudoplastic yielding. *Geochemistry, Geophysics, Geosystems,* 1(8). https://doi.org/10.1029/2000GC000036.

Tackley, P. J. (2000c). Self-consistent generation of tectonics plates in time-dependent, three-dimensional mantle convection simulations: 2. Strain weakening and asthenosphere. *Geochemistry, Geophysics, Geosystems,* 1(8), p. 1026. https://doi.org/10.1029/2000GC000043.

Thielmann, M., & Kaus, B. J. (2012). Shear heating induced lithospheric-scale localization: Does it result in subduction?. *Earth and Planetary Science Letters*, 359, pp. 1-13. https://doi.org/10.1016/j.epsl.2012.10.002.

Twiss, R. (1977). Theory and applicability of a recrystallized grain size paleopiezometer. *Stress in the Earth,* Volume Birkhäuser, Basel, pp. 227-244. https://doi.org/10.1007/978-3-0348-5745-1_13.

Urai, J. L., Means, W. D. & Lister, G. S. (1986). Dynamic recrystallization of minerals. *Mineral and rock deformation,* pp. 161-199. https://doi.org/10.1029/GM036p0161.

Van der Wal, D., Chopra, P., Drury, M., & Gerald, J. F. (1993). Relationships between dynamically recrystallized grain size and deformation conditions in experimentally deformed olivine rocks. *Geophysical Research Letters*, 20(14), pp. 1479-1482. https://doi.org/10.1029/93GL01382.

Van Heck, H. J., & Tackley, P. J. (2008). Planforms of self-consistently generated plates in 3D spherical geometry. *Geophysical Research Letters*, 35(19). https://doi.org/10.1029/2008GL035190.

Weinstein, S. A., & Olson, P. L. (1992). Thermal convection with non-Newtonian plates. *Geophysical Journal International*, 111(3), pp. 515-530. https://doi.org/10.1111/j.1365-246X.1992.tb02109.x.

Zhong, S., Gurnis, M., & Moresi, L. (1998). Role of faults, nonlinear rheology, and viscosity structure in generating plates from instantaneous mantle flow models. *Journal of Geophysical Research: Solid Earth*, 103(B7), pp. 15255-15268. https://doi.org/10.1029/98JB00605.

Figure1.

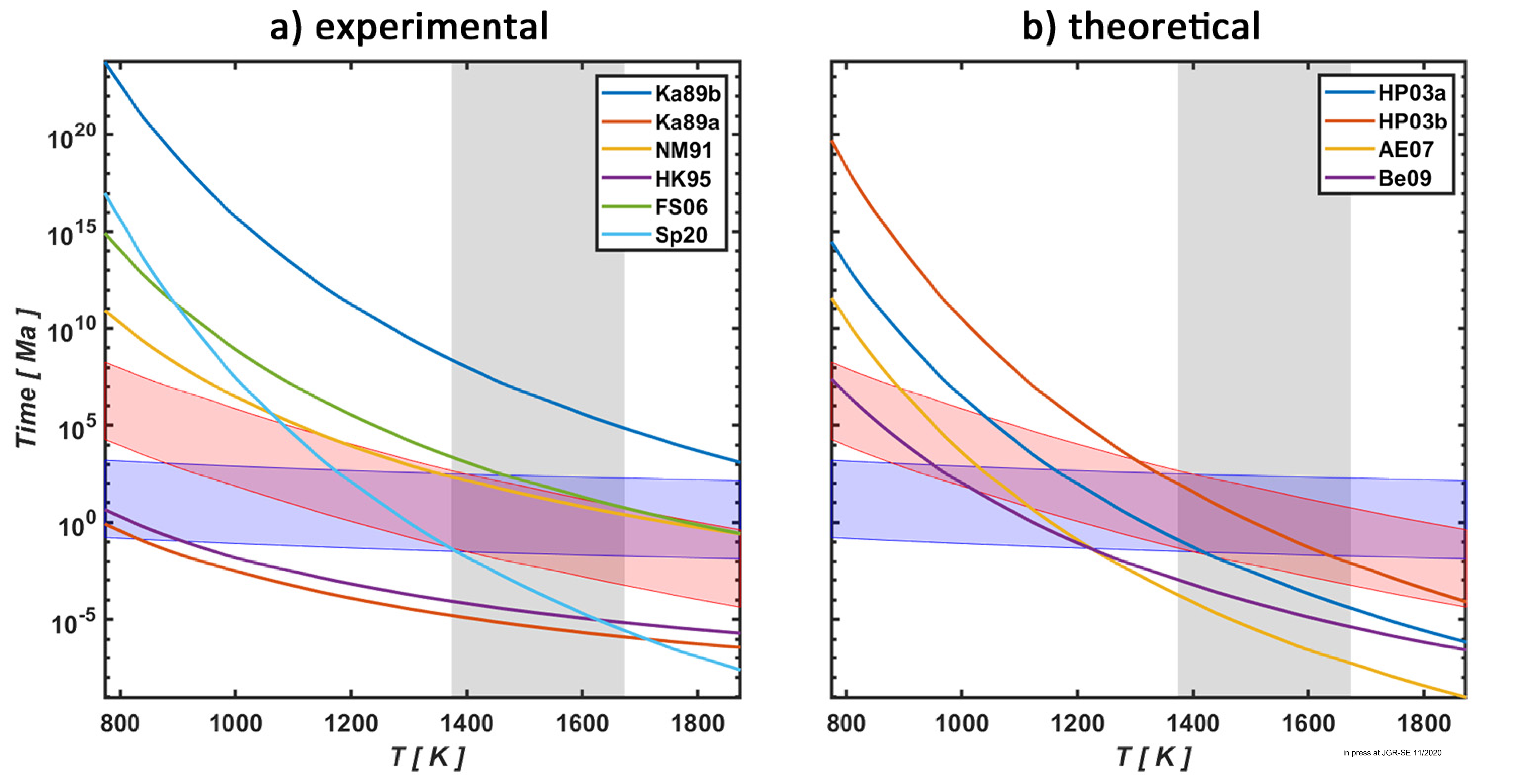
a) experimental
b) theoretical
Ka89b
Ka89a
NM91
HK95
FS06
Sp20
HP03a
HP03b
AE07
Be09
Time [Ma]
10^{20}
10^{15}
10^{10}
10^{5}
10^{0}
10^{-5}
800
1000
1200
1400
1600
1800
T [K]
in press at JGR-SE 11/2020

Figure2.

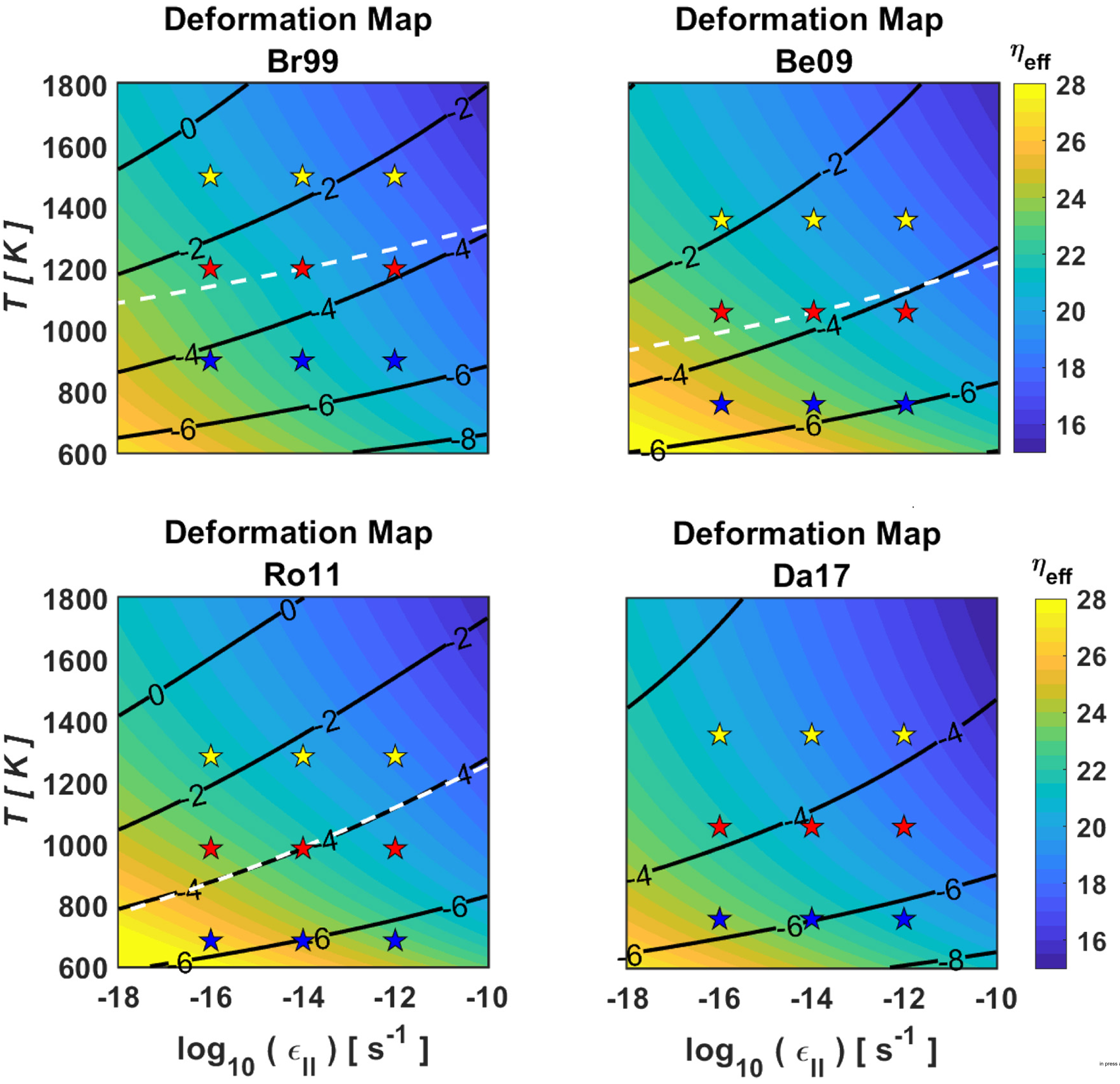

in press at JGR-SE 11/2020

Figure3.

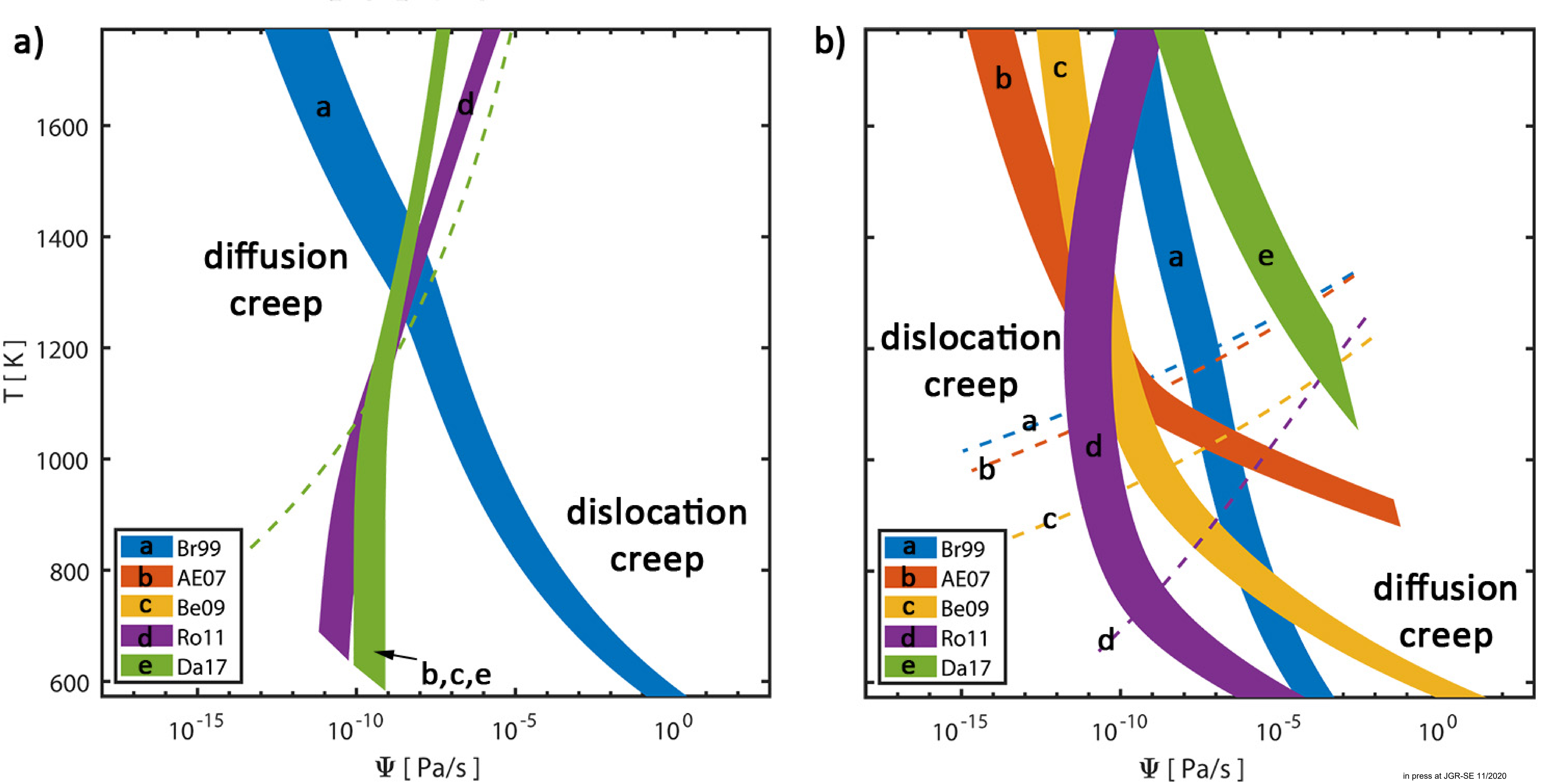

in press at JGR-SE 11/2020

Figure4.

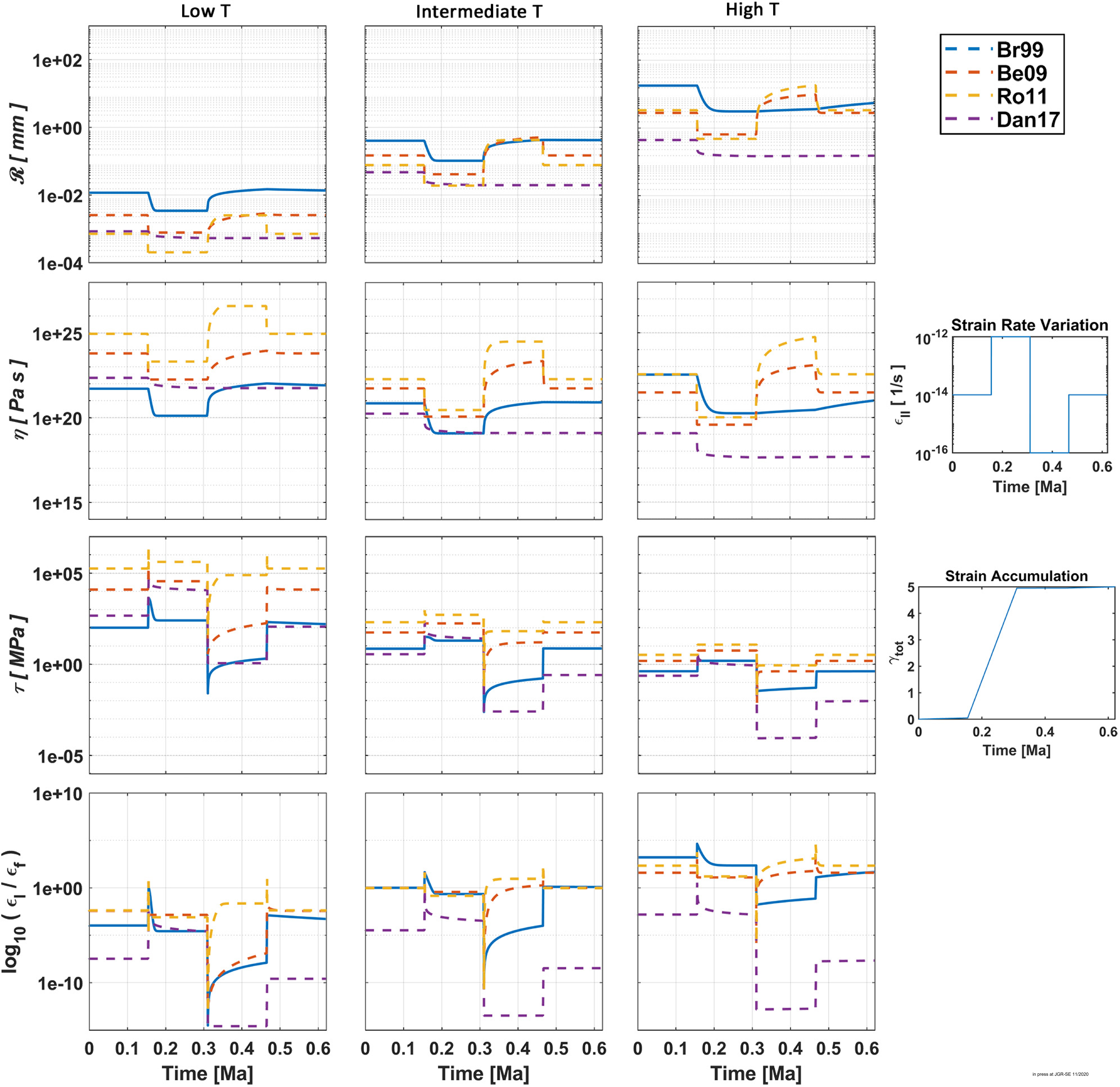

Low T
Intermediate T
High T
Br99
Be09
Ro11
Dan17
ℜ [mm]
η [Pa s]
τ [MPa]
log10 (ε_l / ε_f)
Strain Rate Variation
ε_II [1/s]
Strain Accumulation
γ_tot
Time [Ma]
in press at JGR-SE 11/2020

Figure5.

in press at JGR-SE 11/2020

Figure6.

in press at JGR-SE 11/2020

Figure7.

in press at JGR-SE 11/2020

Figure8.

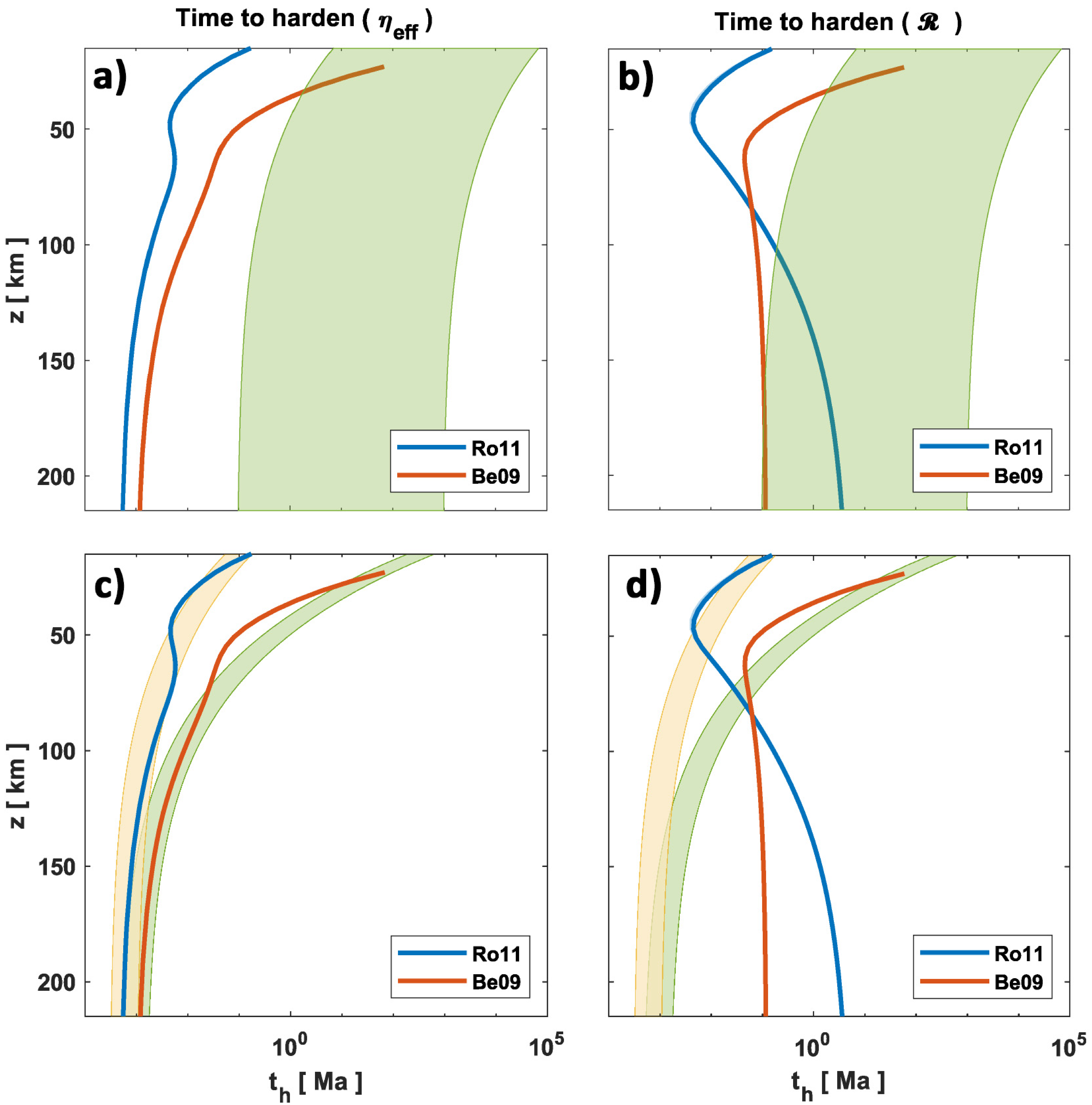

in press at JGR-SE 11/2020